Variability in surface BRDF at different spatial scales (30 m–500 m) over a mixed agricultural landscape as retrieved from airborne and satellite spectral measurements

Miguel O. Román [a,*], Charles K. Gatebe [a,b], Crystal B. Schaaf [c],

Rajesh Poudyal [a,d], Zhuosen Wang [c], and Michael D. King [e]

[a]*NASA Goddard Space Flight Center, Greenbelt, Maryland, USA*

[b]*Goddard Earth Sciences and Technology Center, University of Maryland Baltimore County, Baltimore, Maryland, USA*

[c]*Dept. of Geography and Environment, Boston University, Boston, Massachusetts, USA*

[d]*Science Systems and Applications, Inc., Lanham, MD, USA*

[e]*Laboratory for Atmospheric and Space Physics, University of Colorado, Boulder, Colorado, USA*

* Corresponding author. Tel.: +1 301 614 5498; fax: +1 301 614 5269

E-mail address: Miguel.O.Roman@nasa.gov

Abstract – Over the past decade, the role of multiangle remote sensing has been central to the development of algorithms for the retrieval of global land surface properties including models of the bidirectional reflectance distribution function (BRDF), albedo, land cover/dynamics, burned area extent, as well as other key surface biophysical quantities represented by the anisotropic reflectance characteristics of vegetation. In this study, a new retrieval strategy for fine-to-moderate resolution multiangle observations was developed, based on the operational sequence used to retrieve the Moderate Resolution Imaging Spectroradiometer (MODIS) Collection 5 reflectance and BRDF/albedo products. The algorithm makes use of a semiempirical kernel-driven bidirectional reflectance model to provide estimates of intrinsic albedo (i.e., directional-hemispherical reflectance and bihemispherical reflectance), model parameters describing the BRDF, and extensive quality assurance information. The new retrieval strategy was applied to NASA's Cloud Absorption Radiometer (CAR) data acquired during the 2007 Cloud and Land Surface Interaction Campaign (CLASIC) over the well-instrumented Atmospheric Radiation Measurement Program (ARM) Southern Great Plains (SGP) Cloud and Radiation Testbed (CART) site in Oklahoma, USA. For the case analyzed, we obtained ~1.6 million individual surface bidirectional reflectance factor (BRF) retrievals, from nadir to 75° off-nadir, and at spatial resolutions ranging from 3 m – 500 m. This unique dataset was used to examine the interaction of the spatial and angular characteristics of a mixed agricultural landscape; and provided the basis for detailed assessments of: (1) the use of a priori knowledge in kernel-driven BRDF model inversions; (2) the interaction between surface reflectance anisotropy and instrument spatial resolution; and (3) the uncertainties that arise when sub-pixel differences in the BRDF are aggregated to a moderate resolution satellite pixel. Results offer empirical evidence concerning the influence of scale and spatial heterogeneity in kernel-driven BRDF models; providing potential new insights into the behavior

1

24 and characteristics of different surface radiative properties related to land/use cover change and

25 vegetation structure.

26

31

32

33

34

35

36

37

38

39

40

41

42

43

44

45

46

1. Introduction

Techniques for determining the structure and optical properties of complex heterogeneous environments using multiangle remote sensing are crucial for understanding the effects of environmental change on vegetation structure and thus improve our ability to model terrestrial carbon cycle dynamics and to characterize the ecological functioning of many ecosystems. Recent studies have made considerable progress in developing algorithms for the extraction of quantitative information on terrestrial surface heterogeneity at the subpixel scale (Sandmeier et al. 1998; Widlowski et al. 2001; Pinty et al. 2002; Armston et al. 2007; Chopping et al. 2008; Hill et al. 2008). In general, this has been achieved by examining how different manifestations of the surface reflectance anisotropy over the angular range (e.g., bowl-shape vs. bell-shape anisotropy features) are directly related to canopy physiognomy and structure (e.g. canopy height, size, inter-distance between trees, and background vs. foliage contributions).

In the past, previous experiments have generally followed the central assumption that "the potential to detect structural heterogeneity is independent of the spatial scale corresponding to the pixel size" (Pinty et al. 2002). In line with this assumption, earlier studies have treated satellite BRDF/albedo retrievals as being observed over a homogeneous landscape; thus allowing direct "point-to-pixel" comparisons (Hautecoeur and Leroy 1998; Liang et al. 2002; Jin et al. 2003a; Jin et al. 2003b; Salomon et al. 2006; Chen et al. 2008; Knobelspiesse et al. 2008; Liu et al. 2009; Rutan et al. 2009). Recent studies have further evaluated surface albedo retrievals both in terms of the spatial correspondence (or representativeness) of the field (or tower-based) data and its relationship to the larger satellite pixel (Susaki et al. 2007; Román et al. 2009; Román et al. 2010). However, because of the impact of view and solar zenith angle (SZA) dependencies, sub-grid scale spatial heterogeneity, and other underlying sources of variation that introduce

70   measurement uncertainties within the ground resolution element (GRE) of satellite retrievals; the

71   BRDF (and thus albedo) of certain ecosystems can only be correctly sampled with airborne mul-

72   tiangle measurements (Walthall et al. 2000). Among key biomes affected by these sources of er-

73   ror are mixed-forest canopies (Johnson 1994; Russell et al. 1997b), tropical savannas (Hill et al.

74   2008; Georgiev et al. 2009), shrublands (Chopping et al. 2004), as well as snow-covered envi-

75   ronments (Lyapustin et al. 2009). Furthermore, recent studies contend that subpixel vegetation

76   structure is only detectable when obtaining measurements near the principal plane; i.e., where

77   BRDF effects are most pronounced (Chen et al. 2005). Consequently, the exact nature of these

78   angular-to-structural relationships has been difficult to quantify at the relevant view-angle geo-

79   metries of satellite sensors that routinely sample the BRDF over a single overpass (Leroy et al.

80   1997; Diner et al. 1998b) or in the course of multiple overpasses (Schaaf et al. 2002; Muller et al.

81   2007).

82   Because of the difficulties of estimating, validating, and conveying measurement differenc-

83   es between sensors and in-situ measurements, there is a need to directly examine the accuracy,

84   precision, and uncertainty (APU) of land surface BRDF products; particularly, across complex

85   heterogeneous environments. Accordingly, this study presents a new BRDF/albedo retrieval

86   scheme that uses high quality, multiresolution, and multispectral surface bidirectional reflectance

87   factor (BRF) measurements acquired by NASA's Cloud Absorption Radiometer (CAR) (King et

88   al. 1986; Gatebe et al. 2003). The retrieval strategy, described in Section 2, is based on the opera-

89   tional Moderate Resolution Imaging Spectroradiometer (MODIS) algorithm for retrieving Sur-

90   face Reflectance (Vermote et al. 1997; Kotchenova et al. 2006), BRDF and albedo (Schaaf et al.

91   2002; Schaaf et al. 2011), and was used to examine the two major assumptions underlying semi-

92   empirical kernel-driven BRDF models (Roujean et al. 1992; Lewis 1995; Wanner et al. 1995)

4

93   using data acquired over the well-instrumented Atmospheric Radiation Measurement Program

94   (ARM) Southern Great Plains (SGP) Cloud and Radiation Testbed (CART). The first assumption

95   contends that "linear BRDF models can implicitly model surface heterogeneities." The second

96   one argues that "spatial degradation of modeled bidirectional reflectance can be achieved

97   through degradation of the model parameters describing the BRDF." The first assumption was

98   tested by computing the model-fits error (RMSE) of surface BRDF retrievals acquired directly

99   from CAR data, and then establishing the departure of RMSE values obtained from BRDF re-

100   trievals that employ an ancillary database of a priori archetypal BRDF shapes (*cf.*, Section 4.1).

101   To test the second assumption, the interaction between instrument spatial resolution and surface

102   reflectance anisotropy was examined by assessing the distribution of relative differences in sur-

103   face BRF retrievals obtained from CAR and MODIS BRDF model inversions at different spatial

104   scales and across different spectral regions and view-angle geometries (*cf.*, Section 4.2).

105

106   **2. BRDF/albedo retrieval scheme**

107   The new scheme has three main functional components: atmospheric correction (Fig. 1a),

108   geolocation and gridding (Fig. 1b), and BRDF inversion (Fig. 1c). The aim of atmospheric cor-

109   rection is to retrieve surface-level bidirectional reflectance factor (BRF) measurements from re-

110   motely sensed CAR data, which is contaminated by the effects of atmospheric particles and gases

111   through absorption and scattering of the radiation, especially from the Earth's surface. The aim

112   of geolocation and gridding is to determine the center coordinates of each observation along the

113   instrument scan line (since the CAR data provide only the geolocation of the nadir-looking

114   ground resolution element of each scan), and to register the data to a common grid to maintain

115   consistency across datasets. The aim of BRDF inversion is to fit atmospherically-corrected BRFs

116   to retrieve the RossThick-LiSparseReciprocal (RTLSR) model parameters describing the BRDF

117   in each CAR grid cell and spectral band. The retrieval scheme also performs angular integrations

118   to derive intrinsic land surface albedos for each spectral band, and is supported by extensive

119   quality assurance (QA) information.

120

121   *2.1. Atmospheric correction*

122   In the past, various radiative transfer schemes have been used for the atmospheric correc-

123   tion of CAR data (*cf.*, Gatebe et al., 2003; 2005; Lyapustin et al. 2009). In this study, we used the

124   second simulation of satellite signal in the solar spectrum (6S) model, version 6SV1.1 (Vermote

125   et al. 1997; Kotchenova et al. 2006), which is the heritage model used in the operational MODIS

126   algorithm for retrieving Surface Reflectance. The 6S code is a radiative transfer model based on

127   the successive orders of scattering method. The spectral resolution of the model is 2.5 nm, and

128   the aerosol layer is divided into 13 layers with a scale height of 2 km. The model assumes the

129   atmosphere consists of fixed gases: O_2, O_3, H_2O, CO_2, CH_4, and N_2O. The concentration of O_2,

130   CO_2, CH_4, and N_2O are assumed to be constant and uniformly mixed in the atmosphere. The 6S

131   model allows us to determine the attenuation of solar irradiance under cloudless conditions at the

132   surface. It removes the effects of Rayleigh scattering, aerosol attenuation, and ozone and water

133   vapor absorption, provided we know the key characteristics of the atmosphere, such as the at-

134   mospheric optical thickness, aerosol model, and absorbing gas concentration. Since the CAR

135   measurements were acquired during intensive field campaigns, coincident and co-located

136   ground-based and airborne data needed as input to the 6S model exist. For example, aerosol pa-

137   rameters can be obtained from ground-based sunphotometer measurements (Holben et al. 1998),

138   or from the Ames Airborne Tracking Sunphotometer (Russell et al. 1999), or retrieved from CAR

6

139   measurements (Fig. 1a) (Gatebe et al. 2010).

140

141   *2.2. Geolocation and gridding*

142   Since the CAR has a wide swath (190°) and an instantaneous field of view (IFOV) of 1°,

143   there is a need to determine the center coordinates of each observation ($lat_{off\text{-}nadir}$, $lon_{off\text{-}nadir}$)

144   along the scan line from nadir to near-horizon (i.e., $0° \leq \theta_v \leq 75°$). We used the expression,

145    $$lat_{off-nadir} = \sin^{-1}\left| \sin(lat_{nadir})\cdot \cos\left[\frac{d}{R_\otimes}\right] + \cos(lat_{nadir})\cdot \sin\left[\frac{d}{R_\otimes}\right]\cdot \cos(\phi_v) \right| \tag{1}$$

146    $$lon_{off-nadir} = -\left(a - 360\cdot\left\lfloor\frac{a}{360°}\right\rfloor\right) + 180 \tag{2}$$

147   where:

148    $$d = h\tan(\theta_v) \tag{3}$$

149    $$a = lon_{nadir} - dlon + 180° \tag{4}$$

150    $$dlon = \begin{cases} 0 & \cos(lat_{nadir}) = 0 \\ \psi & \cos(lat_{nadir}) \neq 0 \end{cases} \tag{5}$$

151    $$\psi = \begin{cases} \arctan\left(\dfrac{y}{x}\right) & x > 0 \\ \pi + \arctan\left(\dfrac{y}{x}\right) & y \geq 0, x < 0 \\ -\pi + \arctan\left(\dfrac{y}{x}\right) & y < 0, x < 0 \\ \dfrac{\pi}{2} & y > 0, x = 0 \\ -\dfrac{\pi}{2} & y < 0, x = 0 \\ undefined & y = 0, x = 0 \end{cases} \tag{6}$$

152 $$x = \cos\left[\frac{d}{R_\otimes}\right] - \sin(lat_{nadir}) \cdot \sin(lat_{off-nadir}) \qquad (7)$$

153 $$y = \sin(\phi_v) \cdot \sin\left[\frac{d}{R_\otimes}\right] \cdot \cos(lat_{nadir}) \qquad (8)$$

154 d [km] is the distance from the CAR instrument to the off-nadir target and $R_\otimes$ is the earth's ra-

155 dius $\approx$ 6,378.13 km. The size of the CAR's ground resolution element (GRE), [lat_{nadir}, lon_{nadir}] is

156 a function of the altitude above ground level (h) as well as IFOV of the instrument ($\alpha = 1°$

157 $\approx$17.45 mrad):

158 $$GRE = \alpha \cdot h \qquad (9)$$

159 The ground-projected instantaneous field of view (GIFOV) is then calculated based on the rela-

160 tionship:

161 $$GIFOV = h\left[\tan\left(\theta_v + \frac{\alpha}{2}\right) - \tan\left(\theta_v - \frac{\alpha}{2}\right)\right] \qquad (10)$$

162   Note that the GRE/GIFOV dimensions perpendicular to the azimuth of off-nadir view re-

163 main the same. Each location is also referenced to the WGS-84 datum using a "flat earth" ap-

164 proximation. After establishing the geolocation parameters of each observation (i.e., geographic

165 coordinates, GIFOV, and view-solar geometries), the RTLSR model parameters are then inverted

166 from all available observations on a per grid cell basis. Finally, spatially-distributed (or gridded)

167 fields, each defined by a distinct cell size and GIFOV range, are generated. The end result is a

168 series of multiscale BRDF retrievals derived explicitly from the CAR instrument.

169

170 *2.3. Inversion strategy*

171   For the BRDF inversion, we adapted the operational Moderate Resolution Imaging Spec-

172 troradiometer (MODIS) BRDF/albedo algorithm to fit atmospherically-corrected surface BRF

8

173   data from CAR at any spectral band. The MODIS algorithm makes use of a linear kernel-based

174   model – the semiempirical reciprocal RossThick-LiSparse (RTLSR) model (Wanner et al. 1995;

175   1997; Lucht et al. 2000), which takes the form

$$
\begin{aligned}
BRDF(\theta_s, \theta_v, \Delta\phi, \lambda) &\cong R(\theta_s, \theta_v, \Delta\phi, \Lambda) \\
&= f_{iso}(\Lambda) + f_{vol}(\Lambda)K_{vol}(\theta_s, \theta_v, \Delta\phi) \\
&\quad + f_{geo}(\Lambda)K_{geo}(\theta_s, \theta_v, \Delta\phi, P_4, P_5)
\end{aligned}
\tag{11}
$$

176

177   where:

178
$$
K_{vol} = \frac{(\pi/2 - \xi)\cos\xi + \sin\xi}{\cos\theta_s + \cos\theta_v} - \frac{\pi}{4}
\tag{12}
$$

179
$$
\cos\xi = \cos\theta_s \cos\theta_v + \sin\theta_s \sin\theta_v \cos\Delta\phi
\tag{13}
$$

180
$$
\begin{aligned}
K_{geo} &= \frac{1 + \sec\theta_s' \sec\theta_v' + \tan\theta_s' \tan\theta_v' \cos\Delta\phi}{2} \\
&\quad + \left[\frac{t - \sin t \cos t}{\pi} - 1 \right](\sec\theta_s' + \sec\theta_v')
\end{aligned}
\tag{14}
$$

181
$$
\cos^2 t = \min\left\{ \left[\frac{P_4}{\sec\theta_v' + \sec\theta_s'} \right]^2 \left[D^2 + (\tan\theta_v' \tan\theta_s' \sin\Delta\phi)^2 \right], \ 1 \right\}
\tag{15}
$$

182
$$
\tan\theta_x' = P_5 \tan\theta_x \ ; \ x = v \ or \ s
\tag{16}
$$

183
$$
D = \sqrt{\tan^2\theta_s + \tan^2\theta_v - 2\tan^2\theta_s \tan\theta_v \cos\Delta\phi}
\tag{17}
$$

184   where the wavelength for the narrowband instruments of interest is here defined over the wave-

185   band Λ with limits $[\Lambda_{min}, \Lambda_{max}]$. Parameter $f_{iso}(\Lambda)$ is the isotropic scattering component and

186   equivalent to a nadir-view ($\theta_v = 0$), zenith-sun ($\theta_s = 0$) reflectance retrieval. Parameter $f_{geo}(\Lambda)$ is

187   the coefficient of the LiSparse-Reciprocal geometric scattering kernel K_{geo}, derived for a sparse

188   ensemble of surfaces casting shadows on a Lambertian background (Li and Strahler 1992). Pa-

189   rameter $f_{vol}(\Lambda)$ is the coefficient for the RossThick volume scattering kernel K_{vol}, so called for its

190   assumption of a dense leaf canopy (Ross 1981). $\Delta\phi$ is the relative azimuth angle ($\Delta\phi = \phi_s - \phi_v$)

191   (where subscript s and v denote solar and view azimuth, respectfully) and ξ is the scattering (or

192   phase) angle between sun and view directions. The variable h is the height at which a crown cen-

193   ter is located, b is the vertical half-axis of the modeled ellipsoid, and r is its horizontal radius.

194   Based on previous experiments, the dimensionless crown relative height ($P_4 = h/b$) and shape

195   ($P_5 = b/r$) parameters have been fixed at $h/b = 2$ and $b/r = 1$ to invert the angular radiance data

196   from MODIS (Wanner et al. 1995; Privette et al. 1997).

197   In order to invert Eq. (11) for given reflectance observations $\rho\left(\theta_s^i, \theta_v^i, \Delta\phi^i, \Lambda\right)$ ($i = 1, \ldots, n$)

198   over a given grid cell, we need to minimize $\delta e^2/\delta f_k(\Lambda)$ of a least squares error function

$$
199 \quad e^2 = \frac{1}{n-3} \sum_{i=1}^{n} \frac{\left(\rho\left(\theta_s^i, \theta_v^i, \Delta\phi^i, \Lambda\right) - R\left(\theta_s^i, \theta_v^i, \Delta\phi^i, \Lambda\right)\right)^2}{w_i(\Lambda)} \tag{18}
$$

200   to establish the analytical solution for the RLTSR BRDF model parameter values $f_k(\Lambda)$,

$$
201 \quad f_k(\Lambda) = \sum_{i=1}^{3}\left\{ \sum_{j=1}^{n} \frac{\rho\left(\theta_s^j, \theta_v^j, \Delta\phi^j, \Lambda\right) K_i\left(\theta_s^j, \theta_v^j, \Delta\phi^j, \Lambda\right)}{w_j(\Lambda)} \\ \times \left(\sum_{l=1}^{n} \frac{K_i\left(\theta_s^l, \theta_v^l, \Delta\phi^l, \Lambda\right) K_k\left(\theta_s^l, \theta_v^l, \Delta\phi^l, \Lambda\right)}{w_l(\Lambda)} \right)^{-1} \right\} \tag{19}
$$

202   where $w_j(\Lambda)$ is the weight for the jth observation at waveband Λ. For any given CAR retrieval

203   scenario, a full BRDF model inversion is attempted if at least 7 observations are available. Each

204   observation is evaluated to discard outliers and additional checks (e.g., establishing the model-

205   fits RMSE and angular sampling uncertainty) are performed to assure that the RTLSR model pa-

206   rameters are positive.

207   Fig. 2 illustrates the shapes of the RossThick (K_{vol}) and LiSparseReciprocal (K_{geo}) kernels,

208   based on the CAR atmospherically-corrected BRF data from the CART site, described in Section

209   3. Note that the behavior of the two kernels is different in nature over the full angular range of

210   CAR observations. While they are not perfectly orthogonal functions, K_{vol} and K_{geo} are suffi-

211   ciently independent to allow for a stable recovery of the RTLSR model parameters for many

212   viewing and illumination conditions. The absence of excessive kernel-to-kernel correlation is key

213   to reliable BRDF model inversions (Lucht et al. 2000).

214   Finally, the model-fits error (RMSE)

215   $$RMSE = \sqrt{\frac{\sum_{i=1}^{n}\left(\rho\left(\theta_s^i,\theta_v^i,\Delta\phi^i,\Lambda\right)-R\left(\theta_s^i,\theta_v^i,\Delta\phi^i,\Lambda\right)\times w_i(\Lambda)\right)^2}{n-3}}$$ (20)

216   where $w_i(\Lambda)$ is the weight for the ith observation at waveband Λ. Weights are applied using a

217   standard Gaussian-threshold defined by

218   $$w_i(\Lambda)= p_i(\Lambda)\times s_i(\Lambda)$$ (21)

219   where,

220   $$p_i(\Lambda)= e^{-\frac{\Delta\phi^2}{2c^2}} +e^{-\frac{(180°-\Delta\phi)^2}{2c^2}}$$ (22)

221   $$s_i(\Lambda)= e^{-\frac{(GIFOV-scale)^2}{2d^2}}$$ (23)

222   $$c = 45° \;\; ; \;\; d = scale/3.0$$ (24)

223   The first weight, $p_i(\Lambda)$, depends on the adequacy of the angular sampling across the solar

224   azimuth region or principal plane, where the surface reflectance anisotropy is more sensitive to

225   canopy biophysical characteristics (Privette et al. 1996; Bacour et al. 2002). The second weight,

226   $s_i(\Lambda)$, depends on the degree of spatial correspondence (or representativeness) between the

227   ground-projected instantaneous field of view (GIFOV) and the scale (or grid cell size) being se-

228   lected (Román et al. 2009). The range of viewing and illumination conditions resulting from

11

229   these constraints are intended to produce retrievals that are more sensitive to variability in the

230   structural characteristics of different heterogeneous landscapes.

231   The angular sampling uncertainty is determined by computing the overall spread (or dis-

232   persion, σ_K, of the RTLSR kernels

233    $$\sigma_K = \left[\frac{\sum_{i=1}^{n}(K_{vol}(i) - \overline{K}_{vol})^2}{n-1} + \frac{\sum_{i=1}^{n}(K_{geo}(i) - \overline{K}_{geo})^2}{n-1} \right] \qquad (25)$$

234   Since the RTLSR kernels provide different geometric expressions for a particular type of BRDF,

235   it should follow that the larger the spread (σ_K), the more adequate the angular sampling under a

236   given sun-view geometry.

237   Both the RMSE and angular sampling uncertainty (σ_K) are computed to establish retrieval

238   confidence. Only if the observations pass all of these evaluations is a full inversion performed to

239   establish the RTLSR kernel values that provide the 'best fit' (RMSE) estimate. For those cases

240   with insufficient observations ($i < 7$), or a poor fit, a magnitude inversion is performed rather

241   than a full model inversion. Note that, unlike the MODIS magnitude inversion strategy over

242   snow-free environments (which leverages a global database of archetypal anisotropic models of

243   MODIS-derived representation of seasonal BRDF), this retrieval scheme reutilizes the CAR

244   BRDF retrievals obtained during the same flight period to process those areas where a full re-

245   trieval couldn't be made. An ancillary database derived from high-quality, coincident, and co-

246   located surface BRDF data is then parameterized with area-based proportions of land cover type

247   to obtain a set of archetypal BRDF shapes (*cf.*, Section 3). Consequently, by assuming that sur-

248   face BRFs scale linearly in a spatial sense (Lewis 1995), a full range of mixed BRDF patterns

249   can be reconstructed using the following equation:

250 $$R(\theta_s, \theta_v, \Delta\phi, \Lambda) \cong \sum_{k=1}^{3} f_k'(\Lambda) K_k(\theta_s, \theta_v, \Delta\phi) \qquad (26)$$

251 where

252 $$f_k'(\Lambda) = \sum_{j=1}^{n} c_j f_{k_j}(\Lambda) \qquad (27)$$

253 and c_j is the proportional weight of each land cover type ($j = 1, …, n$) within a given CAR grid

254 cell. Accordingly, magnitude inversions were supported by a "first-guess" estimate of the general

255 BRDF shape for a spatially heterogeneous landscape, and then constrained by the available ob-

256 servations. With the exception of water-contaminated regions, gap-filled retrievals were also ob-

257 tained for areas without available observations.

258

259 *2.3.1. Albedo retrieval*

260 Once appropriate RossThick-LiSparseReciprocal (RTLSR) BRDF model parameters have

261 been retrieved, the directional-hemispherical reflectance (DHR), or black-sky albedo (BSA), are

262 computed at any desired solar zenith angle by integration over all view zenith angles. A further

263 integration over all illumination angles results in a bihemispherical reflectance (BHR), or white-

264 sky albedo (WSA), under isotropic illumination. These two quantities can be determined from

265 Eqn. (28-29):

266 $$BSA(\Lambda, \theta_s) = \sum_k f_k(\Lambda) \cdot h_k(\theta_s) \qquad (28)$$

267 $$WSA(\Lambda) = \sum_k f(\Lambda)_k \cdot H_k \qquad (29)$$

268 where: $h_k(\theta_s)$ is the integral of the BRDF model kernels k over a given view zenith and view-sun

269 relative azimuth angle; H_k is the integral of h_k over a given solar zenith angle θ_s ; and $f_k(\Lambda)$ are

270 the BRDF kernel model parameters k. It should be noted that the black-sky and white-sky albedo

13

271   quantities are intrinsic to a specific location and are governed by the character and structure of its

272   land cover (Schaaf et al. 2008).

273   The CAR retrieval scheme can be extended to acquire other multi-view angle data of in-

274   terest to studies of the photosynthetic and structural characteristics of vegetation covers and their

275   phenological state (e.g., Nadir BRDF-Adjusted Reflectances and BRDF shape indicators). For

276   the purposes of this study, however, only surface BRF retrievals (i.e., obtained from inversion of

277   RTLSR BRDF model parameters) were examined. We can now look at the measurements used to

278   test the new retrieval scheme.

279

280   **3. Measurements**

281   The CAR data were selected from the Cloud and Land Surface Interaction Campaign

282   (CLASIC), an extensive field campaign conducted in the summer of 2007 in Oklahoma and

283   Kansas with a primary emphasis on the US Southern Grain Plains (SGP; Fig. 3a). The intense

284   observing period was from June 9-30, 2007 based out of Ponca City, Oklahoma. In addition to

285   the large-scale soil moisture measurements conducted throughout the CLASIC experiment, land

286   cover surveys, vegetation measurements, and surface characterizations were also conducted to

287   develop detailed vegetation water content and land cover imagery (Cosh 2007). These records

288   were combined with medium-to-high spatial resolution multispectral satellite imagery – i.e., a

289   2.4 m IKONOS scene (GeoEye 2006), three Landsat 30 m scenes and eight Advanced Wide

290   Field Sensor (AWiFS) 56 m scenes (NRSA 2003) – to create a 10 km^2 land cover map with an

291   overall classification accuracy of 92% (relative to ground surveys; Fig. 4a). The effective spatial

292   resolution of the CLASIC land cover map is 2.4 m; although it includes surface characterizations

293   collected at 30 m and 56 m, as well as polygon datasets extracted from land cover surveys. The

294   total number of classes was reduced by 10, according to survey results acquired during the period

295   coinciding with the CAR measurements.

296   Onboard the Jetstream-31 aircraft, the CAR instrument was used to acquire multiangular

297   and multispectral observations under different sky conditions (Fig. 5a,b). Flights were designed

298   to cover four major surface conditions across the SGP, including crops, bare soils, and pasture at

299   the CART site, 36.60°N, 97.48°E, grasslands at the Little Washita Watershed, 35.044°N,

300   97.914°W, irrigated crops at the Fort Cobb Watershed, 35.15°N, -98.47°E, and broadleaf deci-

301   duous canopies at the Forest Site, 35.615°N, -96.07°E) (Cosh 2007). The present study focuses

302   on the events surrounding the CART site, which is heavily instrumented and dominated by cattle

303   pasture, bare soils, and winter-wheat fields (*cf.*, Fig. 3).

304   To acquire BRDF measurements, the aircraft flew a clockwise circular pattern above the

305   surface (Fig. 5c) repeatedly, and at different altitudes ranging from ~0.2 to <8 km. At an aircraft

306   bank angle of 20°, the plane takes roughly 2–3 min to complete an orbit. Among the unique fea-

307   tures of the CAR is the fact that the instrument observes the reflected solar radiation at a fine an-

308   gular resolution defined by an instantaneous field of view of 1°. It is normally set to scan from

309   nadir all the way to the zenith (cf., Fig. 2a), but can also be set to observe the entire downwelling

310   scattered radiation field at approximately half-degree intervals through its 190° aperture at a rate

311   of 100 scans per minute. Therefore, the CAR collects between 76,400 and 114,600 directional

312   measurements of radiance per channel per complete orbit, which amounts to between 687,600

313   and 1,031,400 measurements per orbit for nine channels.

314   We selected the J-31 flight on 24 June 2007, Flight # 1928, over the CART site because of

315   favorable clear-sky conditions. A complete description of this and other CAR flights, including

316   flight summaries (i.e., path, timing, and measurements, imagery, and mission details) can be

317   found on the CAR web site (http://car.gsfc.nasa.gov/). Angular measurements were taken at sev-

318   eral heights above ground level (i.e., 200 m, 600 m, 2000 m, and ~4000 m). This resulted in

319   1,619,543 individual BRDF measurements at view zenith angles from nadir to 75° off-nadir, and

320   at spatial resolutions ranging from 3 m – 500 m. We performed atmospheric correction using

321   each observation's unique viewing (i.e., $0° \leq \Delta\phi \leq 180°$; $0° \leq \theta_v \leq 75°$) and illumination geome-

322   tries (i.e., $48° \leq \theta_s \leq 72°$), under a non-Lambertian surface, and for corresponding height above

323   ground level (i.e., from 0.2 km – 4.0 km). Other quantities used for the radiative transfer calcula-

324   tions include: (1) total column $\tau_{0.55\mu m} = 0.150$ (0.141 above the aircraft when flying at ~0.2 km

325   above the surface); (2) total column $H_2O = 1.42$ g cm^{-2} (0.62 g cm^{-2} above the aircraft); and (3)

326   ozone column amount $O_3 = 344$ DU.

327   A database of archetypal BRDF shapes derived from Flight #1928 measurements, and pa-

328   rameterized with land cover data, was also created. This was achieved by: (1) deriving GIFOV-

329   specific values of percent land cover by using the CLASIC land cover map as the base layer; (2)

330   extracting those observations that formed a single (or dominant) surface condition; and (3) aver-

331   aging those remaining measurements that were acquired at ±15˚ off the principal plane and ob-

332   served under the similar view-solar conditions (i.e., ±1°). We defined dominant surface condi-

333   tions as those with a fractional cover of $\geq 75\%$ and we limited water-contaminated areas to $< 5\%$.

334   To the extent possible, areas comprised by 'water' and 'land/water mix' classes (*cf.*, Fig. 4a)

335   were excluded from this analysis. This was done to reduce classification errors associated with

336   changing weather conditions. The observations that passed the above-mentioned screening tests

337   were then used to invert the RTLSR BRDF model parameters and obtain best-fit (RMSE) esti-

338   mates across the principal plane. Under this premise, the BRDF model parameters acquired using

339   the above mentioned screening process were used to calculate the weighted average (based on

16

340   the band-specific 'best fit' RMSE estimate) for each representative land cover class identified

341   across the CART site during the CLASIC experiment (Table 1).

342   Spatially-distributed BRDF retrievals were derived from the Flight #1928 RossThick-

343   LiSparseReciprocal (RTLSR) model parameters using three different grid sizes. Fig. 6 illustrates

344   the results for a 10 km^2 area surrounding the CART site. Different panels represent the RTLSR

345   kernel values, $f_{iso}(\Lambda)$, $f_{vol}(\Lambda)$, and $f_{geo}(\Lambda)$, for CAR channels $\Lambda = 0.682$ μm (Fig. 6a) and $\Lambda =$

346   0.870 μm (Fig. 6b). Each retrieval is defined by a distinct cell size (or spatial scale) and ground-

347   projected instantaneous field of view (GIFOV) range. The three sampling intervals (i.e., 30 m, 60

348   m, and 240 m) were selected on the basis of how CAR measurements obtained at different GI-

349   FOVs were observed similarly in terms of angular sampling. This is demonstrated in Fig. 7,

350   which shows the distribution of surface-level BRFs from Flight #1928 as a function of GIFOV,

351   view zenith angle, solar zenith angle, and relative azimuth angle. One can see that, irrespective

352   of the spatial scale, CAR observations are sampled across a broad range of viewing and illumina-

353   tion conditions. A slight divergence occurs at observations with GIFOVs > 90 m. Due to a li-

354   mited flight ceiling of ~4 km, the lowest view zenith angle achieved across this particular range

355   was ~30° (Fig. 7b). While this limited view angle range may somewhat affect the quality of the

356   BRDF model inversions at moderate spatial resolutions (i.e., scale = 240 m), a detailed characte-

357   rization of the uncertainties (as described in Section 2.3) was performed to determine whether

358   each retrieval was accessing enough information of the theoretical reflectance space to accurately

359   retrieve the RTLSR model parameters. As a result, retrievals are supported by extensive quality

360   assurance information to make sure that the output is appropriate for validation and inter-

361   comparison purposes.

362   Fig. 6c illustrates the spatial distribution of the Quality Assurance (QA) Science Data Set

363   (SDS) generated by the retrieval scheme. This layer provides basic QA for BRDF model inver-

364   sion data, with green pixels denoting high-quality full inversion retrievals, red pixels denoting

365   moderate quality magnitude inversion retrievals, and yellow pixels denoting gap-filled values

366   (i.e., using the ancillary BRDF database and employing the linear-mixture assumption – *cf.*, Sec-

367   tion 4.1) for areas with insufficient (< 1) observations. Unless a sufficient number of observa-

368   tions (> 7) were available, water-contaminated areas (i.e., black pixels) were not processed. No-

369   tice that the spatial distribution of high-quality (or full inversion) retrievals varies according to

370   the scale of sampling. The 30 m BRDF fields were primarily centered on the CART site, but as

371   the aircraft moved to higher altitudes (i.e., to acquire surface BRFs at GIFOVs > 45 m), more

372   observations were acquired northwest of the site. Despite this effect, a sufficient number of full

373   inversion retrievals (totaling an area of ~4.5 km^2) were observed similarly in terms of spatial and

374   angular sampling. Note that, since the gap-filled BRDF retrievals from CAR are spatially-

375   invariant by nature (i.e., regardless of scale, the resulting mixture of BRDFs originate from the

376   same source) these retrievals were only used to improve the spatial coverage. Accordingly, only

377   full inversion retrievals were used to perform the multiscale comparisons and uncertainty analys-

378   es presented in the discussion (i.e., Section 4.0).

379   During the CLASIC experiment, the number of cloud-free acquisitions from the MODIS

380   sensors onboard the Terra and Aqua satellites was impacted by the anomalous rainfall (Bindlish

381   et al. 2009; Heathman et al. 2009). Since the MODIS Collection 5 BRDF/albedo algorithm as-

382   sumes the surface reflectance anisotropy to remain stable for a period of 16 days, high-quality

383   full inversion retrievals were obtained for less than 20% of the total 10 km^2 study area. To ad-

384   dress the extensive data gaps caused by persistent clouds, gap-free, quality-enhanced retrievals

18

385 (Zhang 2008) were used to reconstruct the surface reflectance anisotropy of the CART site dur-

386 ing the CLASIC experiment. By applying temporal fitting techniques based on vegetation yearly

387 development and spatial fitting techniques to the MODIS RTLSR BRDF model inversions –

388 similar to the techniques previously applied to the MODIS albedo products (Moody et al. 2008)

389 and the MODIS leaf area index (LAI) products (Gao et al. 2008) – this approach was able to

390 compensate for missing data and provide an estimate of the surface reflectance anisotropy for

391 situations under cloud-contaminated conditions. It is important to note, however, that despite the

392 usefulness of this retrieval method in maximizing the influence of available observations, the re-

393 sulting BRDF fields can only provide a close (but not exact) representation of the surface condi-

394 tions during the CLASIC experiment. Thus it is difficult to determine, through this approach,

395 whether rapidly changing surface conditions resulting from flooding and agricultural activities

396 are being captured completely and accurately throughout this period. Nevertheless, a judicious

397 use of available in-situ and ancillary datasets should provide sufficient constrains to address land

398 cover/use changes resulting from events following Flight #1928.

399

400

401 **4. Discussion**

402   The purpose of this section is to demonstrate results from the new BRDF retrieval scheme

403 with inversion of data from the CLASIC experiment. We will also examine the uncertainties in

404 BRDF retrievals resulting from utilization of a priori knowledge in kernel-driven BRDF model

405 inversions, explore the spatial scaling assumptions, and finally compare the CAR and MODIS

406 BRDF retrievals.

407

4.1. A priori knowledge in kernel-driven BRDF model inversion

409   Routine production of land surface BRDF retrievals is often achieved by compiling (or re-

410   lying on) a global database of archetypal BRDFs that seeks to describe the natural variability of

411   terrestrial ecosystems, at several seasons whenever possible (Bicheron and Leroy 2000; Strugnell

412   et al. 2001; Lacaze et al. 2002; Bacour and Bréon 2005). In general, the BRDF associated with

413   each location is assumed to be comprised of either a "complete" linear mixture of different eco-

414   system types or "dominated" by a single ecosystem type. In other cases, target−specific BRDF

415   knowledge is used to supplement available observations and improve the quality of a retrieval.

416   For instance, Jin et al., (2002) has leveraged the BRDF model parameters derived from Multi-

417   angle Imaging SpectroRadiometer (MISR) surface BRFs to bring additional information to the

418   MODIS retrieval scheme; especially when the MISR observations were close to the principal

419   plane. In either case (i.e., using land cover type−related knowledge or target−specific know-

420   ledge), a priori information is being used to indicate when retrieved RTLSR model parameters

421   (or albedos) are outside the expected bounds. These approaches are based on Bayesian inference

422   theory, which is considered to be the best way to make use of a priori knowledge to yield a post-

423   eriori estimates of unknown BRDF model parameters (Li et al. 2001).

424   We now examine the efficiency of BRDF retrievals employing a priori archetypal BRDF

425   shapes to describe the surface anisotropy as either: (1) a linear-mixture of different ecosystem

426   types; or (2) a single (or dominant) ecosystem type. The goal of this exercise is to provide addi-

427   tional constrains into the appropriate spatial length scales and degree of subpixel detail necessary

428   to retrieve the BRDF of target using land cover type−related knowledge. Using data from Flight

429   #1928, we computed the model-fits error (RMSE) of high-quality full inversion retrievals ac-

430   quired directly from CAR data and then established the relative departure of RMSE values

431   (%)using the "linear-mixture" (i.e., ΔRMSE = RMSE Linear-Mixture – RMSE Full Inversion)

432   and "dominant" (i.e., ΔRMSE = RMSE Dominant – RMSE Full Inversion) approaches (Fig. 8;

433   Table 2). Since the RMSE establishes the deviation of the RTLSR model-fits from actual surface

434   BRF measurements, this evaluation should result in uncertainty estimates that are of equal (or

435   comparable) magnitude to those derived through direct means (i.e., from high-quality, full inver-

436   sion retrievals). Thus, if BRDF retrievals employing a priori archetypal BRDF shapes can truly

437   characterize the reflectance anisotropy of mixed agricultural landscape, then the cumulative dis-

438   tribution of relative RMSE differences (%) should follow a normal pattern with a limit (ΔRMSE)

439   equal or close to zero. Note that, based on the scaling principles of linear BRDF modeling

440   theory, this should apply regardless of the scale at which the assumption is being examined.

441   Results confirm that the relative RMSEs for a priori archetypal BRDF shapes are mod-

442   erately higher than the full-inversion results. The uncertainties are also consistently larger in the

443   shorter wavelengths ($\Lambda \leq 0.682$ μm) and smaller at the longer wavelengths ($\Lambda \geq 0.870$ μm). Im-

444   provements in the range of 0.5% – 6.5% (relative RMSE terms) were also documented when re-

445   placing the "single-biome" BRDFs with the "linear-mixture" BRDFs. Finally, with the exception

446   of the blue CAR channel ($\Lambda = 0.472$ μm), retrievals at coarser spatial resolutions (i.e., > 90 m)

447   were consistently of higher quality than those retrieved at finer spatial resolutions (i.e., < 45 m).

448   Thus, while the utilization of a priori knowledge obtained at fine spatial scales is usually as-

449   sumed to capture the angular variability of spatially heterogeneous environments, these results

450   suggest that the assumption of linearity in kernel-driven BRDF models may in fact be most ap-

451   propriate at "landscape-level" scales (i.e., > 90 m).

452

453

21

454 *4.2. Spatial scaling assumption*

455   Due to constraints of instrumentation, platform, and the logistically-challenging nature of

456 airborne data collection and processing, most airborne multiangle experiments have been unable

457 to acquire spatially-distributed BRDF data at landscape-level scales > 90 m (Walthall et al.

458 2000). To get around this problem, previous studies have stipulated that in-situ measurements

459 acquired at scales larger than the intrinsic length scale of the surface should represent the BRDF

460 patterns observed at larger spatial scales (Brown de Colstoun et al. 1996; Leroy et al. 1997; Qin

461 and Gerstl 2000). In general, a GIFOV ≥ 15 m has been routinely used to provide an adequate

462 sample of the BRDF at subpixel scales (Pelgrum et al. 2000; Chopping et al. 2002). Thus, up to

463 now, the only alternative has been to "simulate" a larger GIFOV by convolving fine-resolution

464 estimates with the point spread function (PSF) of a moderate resolution satellite sensor. For in-

465 stance, the AirMISR instrument with an effective pixel size of 27.5 m at nadir, which grows at

466 steeper angles (Diner et al. 1998a), is upscaled to match MISR's effective spatial resolution of

467 275 m (Gobron et al. 2002; Pinty et al. 2002). The same spatial scaling principle is applied to the

468 MODIS Airborne Simulator (MAS) (King et al. 1996), which has an effective pixel size of 50 m,

469 and is upscaled to MODIS spatial resolutions >250 m. The assumption, then, is that the aggre-

470 gated BRDF datasets should scale linearly in a spatial sense (Roujean et al. 1992; Lewis 1995).

471 However, because the scale for shadowing and clumping effects depends on spatial resolution,

472 such "upscaled" results can lead to different spatial and structural patterns (d'Entremont et al.

473 1999; Walthall et al. 2000). As a result, high spatial resolution BRDF retrievals that are con-

474 volved to a larger GIFOV may still be conditioned by the BRDF patterns observed at plot-level

475 scales. To illustrate this effect, Fig. 9 illustrates the spatial and angular characteristics of CAR

476 and MODIS Collection 5 BRDF model inversions (MCD43A1). Each false-color composite de-

477   scribes the spectral BRF response at 0.870 µm (Red), 0.682 µm (Green), and 0.472 µm (Blue),

478   for five different view zenith angle intervals measured across the principal plane (i.e., $\Delta\phi = 0°$)

479   and using a SZA = 60°. Negative VZA values represent the backscattering while positive values

480   represent the forward scattering. In the back scattering direction, pastures and crop fields show a

481   strong directional response in the NIR (as seen in bright-reds and pink colors); while bare soils

482   show a lower directional response (as seen by shades of pale-blue and cyan). Conversely, in-

483   creased shadowing in the forward scattering results in a lower response in the red and NIR (as

484   seen in dark purple and magenta tones), which then increases the overall contrast of bare soils (as

485   seen in dark and bright shades of cyan). The histograms in Fig. 10 illustrate the distribution for

486   each of the view-angle geometries examined in Fig. 9, using four discreet wavelengths from

487   0.472 µm (0.465 µm for MODIS) to 1.219 µm (1.241 µm for MODIS). Results show a good de-

488   gree of correspondence between CAR and MODIS BRFs at view angles closer to nadir (i.e., -30°

489    $\leq$ VZA $\leq$ +30°), with improved results for wavelengths $\leq$ 0.682 µm. However, at high view ze-

490   nith angles, the spread of the distribution in the BRF tends to be narrower at spatial scales $\leq$ 60 m

491   and broader at scales $\geq$ 240 m. At landscape-level scales, this results in higher BRF values across

492   the backscattering and lower BRF values across the forward scattering directions. Conversely, at

493   scales $\leq$ 60 m, vegetated areas exhibit a strong directional response in the forward scattering, and

494   (with the exception of the 1.219 µm channel) appear darker in the backscattering. These scaling

495   effects may result from distinct spatial and structural BRDF patterns, including: (1) subpixel dif-

496   ferences in the BRDF (e.g., row and close-grown crops or mosaics of crops with natural vegeta-

497   tion) observed at spatial resolutions > 90 m, which decreases the overall slope of the BRDF

498   shape at moderate spatial resolutions; (2) the influence of specular reflection and transmission of

23

499   light at spatial resolutions ≤ 60 m; and (3) the fundamental scales of shadowing for foliage and

500   canopy components manifested at spatial resolutions > 90 m.

501   In order to quantify the uncertainties that arise when sub-pixel differences in the BRDF are

502   aggregated to a moderate resolution satellite pixel, the quality of MODIS RTLSR surface BRF

503   retrievals was evaluated across spatial scales. Results in Table 3 show that the MODIS retrievals

504   are more consistent with CAR-derived BRFs at moderate spatial resolutions (i.e., scale = 240 m).

505   The quality of these direct "moderate pixel-to-moderate pixel" comparisons resulted in APU

506   units that were 1.15% more accurate, 3.59% more precise, and 0.005 less uncertain. While the

507   finer scale CAR BRFs (i.e., scale = 30 m) were, at times, as consistent as the 240 m BRDF

508   fields, the intermediate results (i.e., scale = 60 m) were not as reliable. The most significant im-

509   provement resulted from the ability of moderate resolution retrievals from CAR to capture the

510   range of mixed BRDF patterns as observed by a MODIS 500 m grid cell. This resulted in more

511   precise (and thus, less uncertain) estimates.

512

513   **5. Conclusions**

514   In previous aircraft campaigns using a variety of multiangular sensors, e.g., FIFE (Sellers

515   et al. 1988; Sellers et al. 1992), OTTER (Waring and Peterson 1994), HAPEX-Sahel (Goutorbe

516   et al. 1994), BOREAS (Russell et al. 1997a), PROVE (Privette et al. 2000), and SAFARI 2000

517   (Swap et al. 2002; Privette et al. 2004) it was common to acquire multiangle surface bidirectional

518   reflectance factor (BRF) measurements and then compare them directly against coincident

519   ground and/or satellite data to obtain information on both the structure and functioning of terre-

520   strial ecosystems. As we note, these "point-to-pixel" comparisons are influenced by very distinct

521   spatial and structural patterns, including: (1) subpixel differences in the BRDF observed at spa-

24

522   tial resolutions > 90 m; (2) the influence of specular reflection and transmission of light at spatial

523   resolutions < 90 m; and (3) the fundamental scales of shadowing for foliage and canopy compo-

524   nents manifested at spatial resolutions > 90 m. These scaling mechanisms, as well as other mea-

525   surement uncertainties arising from geospatial aggregation of subpixel vegetation structural cha-

526   racteristics, can have potential impacts on the utility of multiangle data and products to charac-

527   terize the ecological and biophysical state of complex ecosystems. Perhaps the biggest problem

528   thus far has been the lack of adequate in-situ measurements and validation techniques for acquir-

529   ing spatially-distributed surface BRDF data at the relevant spatial scales at which global land

530   products are commonly utilized. While airborne measurements are commonly used to provide an

531   intermediate scale between plot-level (< 15 m) and landscape-level (> 90 m) measurements, the

532   results from this work confirm that, as a result of the inherent lack of mixed-pixel sampling (i.e.,

533   both in spatial and angular sense), such approaches are not as appropriate for multiangle remote

534   sensing studies.

535   With its unique design (i.e., a 190° swath, 1° IFOV, oversampling every 0.5° along the ver-

536   tical plane), unparalleled instrument accuracy ($\leq 5\%$), and flight capabilities (i.e., multiple circu-

537   lar patterns achieved at different heights above ground level under clear-sky conditions),

538   NASA's Cloud Absorption Radiometer (CAR) is used to generate spatially-distributed BRDF

539   products at different spatial scales. To demonstrate this capability, a new retrieval scheme was

540   developed and applied to a single flight dataset containing ~1.6 million individual surface BRFs

541   obtained at view zenith angles from nadir to 75° off-nadir, and at spatial resolutions ranging from

542   3 m – 500 m. Results over a 10 km^2 area centered on the well-instrumented CART site were then

543   used to determine whether the ability of kernel-driven BRDF models to detect measures of cano-

544   py physiognomy and structure (e.g., through different manifestations of the surface reflectance

545 anisotropy over the angular range) is independent of the spatial resolution of acquisition. As-

546 sessments between BRDF retrievals acquired from CAR at different spatial scales, and between

547 CAR and MODIS (500 m) retrievals, confirm that while BRDF patterns observed at fine spatial

548 resolutions (i.e., ~15 m) are usually assumed to be large enough to capture the intrinsic length

549 scale of the surface, the utilization of a priori knowledge in kernel-driven BRDF model inver-

550 sions and the spatial scaling assumptions underlying semi-empirical kernel-driven BRDF models

551 (Roujean et al. 1992; Lewis 1995) may in fact be limited to considerably larger scales. Thus, on-

552 ly by acquiring surface BRDF retrievals at "landscape-level" scales (i.e., > 90 m) can a resolu-

553 tion limit be reached whereby the resulting BRDF patterns are still representative of the structur-

554 al response of complex ecosystems at the scale of moderate resolution satellite sensors. Nonethe-

555 less, further research is needed (particularly over landscapes with two-layer mixtures of woody

556 overstory and herbaceous understory) to establish more definitive limits on the accuracy of these

557 scaling assumptions. This would allow us to determine what kind of variability in the BRDF is

558 important at what kind of scales.

559   With the advent of a new generation of multi-sensor data and products obtained through fu-

560 sion of high-spatial resolution (e.g., Landsat TM/ETM+) and high-temporal resolution satellite

561 datasets (e.g., MODIS and in the future VIIRS) (Gao et al. 2006; Roy et al. 2008), recent efforts

562 have explored the "MODISization" of nadir-looking satellite sensors to obtain high-resolution

563 (30 m) MODIS-driven surface biophysical products at shorter temporal scales (i.e., from weeks

564 to days). Earlier schemes have taken advantage of the temporal efficiency of MODIS (500 m)

565 BRDF retrievals to (among several things) extrapolate the peak-growing season estimates of LAI

566 and/or derive spatially-complete (or gap-filled) directional reflectance retrievals for missing

567 dates of acquisition. This study demonstrates a unique BRDF retrieval capability that may well

26

568   serve research efforts that seek to evaluate and refine the accuracy of these multisensor data and

569   products. As more campaign datasets become available in the near future, BRDF retrievals from

570   CAR will be used to obtain different albedo, angular, and vegetation quantities, including BRDF

571   shape indicators (Hill et al. 2008), foliage clumping index (CI) (Chen 1996), canopy shadow

572   fraction, and top-of-canopy vegetation indexes (i.e., NDVI and EVI) (Tucker 1979; Huete et al.

573   2002) derived from Nadir BRDF-Adjusted Reflectances (NBAR) (Schaaf et al. 2002). In addi-

574   tion to algorithm refinement and validation exercises, these retrievals can be potentially used to

575   characterize the structural dynamics of complex heterogeneous environments, also providing

576   much needed constraints to model interpolations/extrapolations from multisensor surface bio-

577   physical datasets obtained at different spatial scales and time periods.

578   These reference datasets are also needed for studies seeking to identify systematic differ-

579   ences between satellite sensors that may affect the quality and consistency of long-term Earth

580   system data records. For instance, satellite intercomparisons, while useful in pointing out areas of

581   divergence, both in terms of value and quality assurance, cannot establish what products are cor-

582   rect without an independent benchmark that is able to reproduce the wide range of view-angle

583   geometries and retrieval schemes employed by multiple BRDF/albedo datasets (Muller et al.

584   2007; Geiger et al. 2008; Rutan et al. 2009; Pinty et al. 2010; Taberner et al. 2010). Without an

585   independent mechanism, these assessments will continue to be limited to some verification of the

586   relative performance.

587

588   **Acknowledgements**

597

References

599   Armston, J.D., Scarth, P.F., Phinn, S.R., & Danaher, T.J. (2007). Analysis of multi-date
600   MISR measurements for forest and woodland communities, Queensland, Australia. *Remote Sens-*
601   *ing of Environment, 107*, 287-298.

602   Bacour, C., & Bréon, F.M. (2005). Variability of biome reflectance directional signatures as
603   seen by POLDER. *Remote Sensing of Environment, 98*, 80-95.

604   Bacour, C., Jacquemoud, S., Leroy, M., Hautecoeur, O., Weiss, M., Prévot, L., Brugueir, N.,
605   & Chauki, H. (2002). Reliability of the estimation of vegetation characteristics by inversion of
606   three canopy reflectance models on airborne polder data. *Agronomie, 22*, 555-565.

607   Bicheron, P., & Leroy, M. (2000). Bidirectional reflectance distribution function signatures
608   of major biomes observed from space. *Journal of Geophysical Research, 105*, 26669-26681.

609   Bindlish, R., Jackson, T., Sun, R., Cosh, M., Yueh, S., & Dinardo, S. (2009). Combined pas-
610   sive and active microwave observations of soil moisture during CLASIC. *IEEE Geoscience and*
611   *Remote Sensing Letters, 6*, 644-648, doi: 10.1109/LGRS.2009.2028441.

612   Brown de Colstoun, E.C., Walthall, C.L., Cialtela, A.T., Vermote, E.R., Halthore, R.N., &
613   Irons, J.R. (1996). Variability of BRDF with land cover type for the west central HAPEX Sahel
614   super site. In, *Proceedings of the International Geoscience and Remote Sensing Symposium,*
615   *IGARSS'96*. Lincoln, Nebraska USA.

616   Chen, J.M. (1996). Optically-based methods for measuring seasonal variation of leaf area
617   index in boreal conifer stands. *Agricultural and Forest Meteorology, 80*, 135-163.

618   Chen, J.M., Menges, C.H., & Leblanc, S.G. (2005). Global mapping of foliage clumping in-
619   dex using multi-angular satellite data. *Remote Sensing of Environment, 97*, 447-457.

620   Chen, Y., Liang, S., Wang, J., Kim, H., & Martonchik, J.V. (2008). Validation of the MISR
621   land surface broadband albedo. *International Journal of Remote Sensing, 29*, 6971-6989.

622   Chopping, M., Su, L., Rango, A., Martonchik, J.V., Peters, D.P.C., & Laliberte, A. (2008).
623   Remote sensing of woody shrub cover in desert grasslands using MISR with a geometric-optical
624   canopy reflectance model. *Remote Sensing of Environment, 112*, 19-34,
625   10.1016/j.rse.2006.04.023.

626   Chopping, M.J., Rango, A., Havstad, K.M., Schiebe, F.R., Ritchie, J.C., Schmugge, T.J.,
627   French, A.N., Su, L., McKee, L., & Davis, M.R. (2002). Canopy attributes of desert grassland
628   and transition communities derived from multiangular airborne imagery. *Remote Sensing of En-*
629   *vironment, 85*, 339-354.

630   Chopping, M.J., Su, L., Rango, A., & Maxwell, C. (2004). Modelling the reflectance aniso-
631   tropy of Chihuahuan Desert grass-shrub transition canopy-soil complexes. *International Journal*
632   *of Remote Sensing, 25*, 2725-2745.

633   Cosh, M.H. (2007). SGP Cloud and Land Surface Interaction Campaign (CLASIC) Land
634   Surface States and Fluxes Experiment Plan. In: Atmospheric Radiation Measurement (ARM)
635   Program.

636   d'Entremont, R.P., Schaaf, C.B., Lucht, W., & Strahler, A.H. (1999). Retrieval of red spec-
637   tral albedo and bidirectional reflectance using AVHRR HRPT and GOES satellite observations
638   of the New England region. *Journal of Geophysical Research, 104*, 6229-6239.

639   Diner, D.J., Barge, L.M., Bruegge, C.J., Chrien, T.G., Conel, J.E., Eastwood, M.L., Garcia,
640   J.D., Hernandez, M.A., Kurzweil, C.G., Ledeboer, W.C., Pignatano, N.D., Sarture, C.M., &
641   Smith, B.G. (1998a). Airborne Multi-angle Imaging SpectroRadiometer (AirMISR) - Instrument
642   description and first results. *IEEE Transactions on Geoscience and Remote Sensing, 36*, 1339-
643   1349, doi:10.1109/36.701083

644   Diner, D.J., Beckert, J.C., Reilly, T.H., Bruegge, C.J., Conel, J.E., Kahn, R.A., Martonchik,
645   J.V., Ackerman, T.P., Davies, R., Gerstl, S.A.W., Gordon, H.R., Muller, J.P., Myneni, R.B., Sel-
646   lers, P.J., Pinty, B., & Verstraete, M.M. (1998b). Multi-angle Imaging SpectroRadiometer
647   (MISR) - Instrument description and experiment overview. *IEEE Transactions on Geoscience*
648   *and Remote Sensing, 36*, 1072-1087.

649   Gao, F., Masek, J., Schwaller, M., & Hall, F. (2006). On the blending of the Landsat and
650   MODIS surface feflectance: Predicting daily Landsat surface reflectance. *IEEE Transactions on*
651   *Geoscience and Remote Sensing, 44*, 2207-2218.

652   Gao, F., Morisette, J.T., Wolfe, R.E., Ederer, G., Pedelty, J., Masuoka, E., Myneni, R., Tan,
653   B., & Nightingale, J. (2008). An algorithm to produce temporally and spatially continuous
654   MODIS LAI time series. *IEEE Geoscience and Remote Sensing Letters, 5*, 60-64.

655   Gatebe, C.K., Dubovik, O., King, M.D., & Sinyuk, A. (2010). Simultaneous retrieval of
656 aerosol and surface optical properties from combined airborne-and ground-based direct and dif-
657 fuse radiometric measurements. *Atmospheric Chemistry and Physics, 10*, 2777-2794.

658   Gatebe, C.K., King, M.D., Platnick, S., Arnold, G.T., Vermote, E.F., & Schmid, B. (2003).
659 Airborne spectral measurements of surface-atmosphere anisotropy for several surfaces and eco-
660 systems over southern Africa. *Journal of Geophysical Research, 108(D13)*,
661 doi:10.1029/2002JD002397.

662   Geiger, B., Carrer, D., Franchistéguy, L., Roujean, J.L., & C.Meurey (2008). Land surface
663 albedo derived on a daily basis from Meteosat second generation observations. *IEEE Transac-*
664 *tions on Geoscience and Remote Sensing, 46*, 3841-3856.

665   GeoEye (2006). IKONOS Imagery Products Guide Version 1.5. In. Dulles, VA.

666   Georgiev, G.T., Gatebe, C.K., Butler, J.J., & King, M.D. (2009). BRDF analysis of savanna
667 vegetation and salt-pan samples. *IEEE Transactions on Geoscience and Remote Sensing, 47*,
668 2546-2556.

669   Gobron, N., Pinty, B., Verstraete, M.M., Widlowski, J.-L., & Diner, D. (2002). Uniqueness
670 of multiangular measurements—Part II: Joint retrieval of vegetation structure and photosynthetic
671 activity from MISR. *IEEE Transactions on Geoscience and Remote Sensing, 40*, 1574-1592.

672   Goutorbe, J.-P., Lebel, T., Tinga, A., Bessemoulin, P., Brouwer, J., Dolman, A.J., Engman,
673 E.T., Gash, J.H.C., Hoepffner, M., Kabat, P., Kerr, Y.H., Monteny, B., Prince, S., Said, F., Sel-
674 lers, P., & Wallace, J.S. (1994). HAPEX-Sahel: a large-scale study of land-atmosphere interac-
675 tions in the semi-arid tropics. *Annales Geophysicae, 12*, 53-64.

676   Hautecoeur, O., & Leroy, M.M. (1998). Surface bidirectional reflectance distribution func-
677 tion observed at global scale by POLDER/ADEOS. *Geophysical Research Letters, 25*, 4197-
678 4200.

679   Heathman, G.C., Larose, M., Cosh, M.H., & Bindlish, R. (2009). Surface and profile soil
680 moisture spatio-temporal analysis during an excessive rainfall period in the Southern Great
681 Plains, USA. *CATENA, 78*, 159-169, DOI: 10.1016/j.catena.2009.04.002.

682   Hill, M.J., Averill, C., Jiao, Z., Schaaf, C.B., & Armston, J.D. (2008). Relationship of MISR
683 RPV parameters and MODIS BRDF shape indicators to surface vegetation patterns in an Aus-
684 tralian tropical savanna. *Canadian Journal of Remote Sensing, 34*, S247-S267.

685   Holben, B.N., Eck, T.F., Slutsker, I., Tanré, D., Buis, J.P., Setzer, A., Vermote, E., Reagan,
686 J.A., Kaufman, Y.J., Nakajima, T., Lavenu, F., Jankowiak, I., & Smirnov, A. (1998). AERO-

NET–A federated instrument network and data archive for aerosol characterization. *Remote Sensing of Environment, 66*, 1-16.

Huete, A., Didan, K., Miura, T., Rodriguez, E.P., Gao, X., & Ferreira, L.G. (2002). Overview of the radiometric and biophysical performance of the MODIS vegetation indices. *Remote Sensing of Environment, 83*, 195-213.

Jin, Y., Schaaf, C.B., Gao, F., Li, X., Strahler, A.H., Bruegge, C., & Martonchik, J. (2002). Improving MODIS surface BRDF/Albedo retrieval with MISR multi-angle observations. *IEEE Transactions on Geoscience and Remote Sensing, 40*, 1593-1604.

Jin, Y.F., Schaaf, C.B., Gao, F., Li, X.W., Strahler, A.H., Lucht, W., & Liang, S.L. (2003a). Consistency of MODIS surface bidirectional reflectance distribution function and albedo retrievals: 1. Algorithm performance. *Journal of Geophysical Research-Atmospheres, 108*, D5.

Jin, Y.F., Schaaf, C.B., Woodcock, C.E., Gao, F., Li, X.W., Strahler, A.H., Lucht, W., & Liang, S.L. (2003b). Consistency of MODIS surface bidirectional reflectance distribution function and albedo retrievals: 2. Validation. *Journal of Geophysical Research-Atmospheres, 108*, D5.

Johnson, L.F. (1994). Multiple view zenith angle observations of reflectance from ponderosa pine stands. *International Journal of Remote Sensing, 15*, 3859-3865.

King, M.D., Menzel, W.P., Grant, P.S., Myers, J.S., Arnold, G.T., Platnick, S.E., Gumley, L.E., Tsay, S.-C., Moeller, C.C., Fitzgerald, M., Brown, K.S., & Osterwisch, F.G. (1996). Airborne scanning spectrometer for remote sensing of cloud, aerosol, water vapor and surface properties. *Journal of Atmospheric and Oceanic Technology, 13*.

King, M.D., Strange, M.G., Leone, P., & Blaine, L.R. (1986). Multiwavelength scanning radiometer for airborne measurements of scattered radiation within clouds. *Journal of Atmospheric and Oceanic Technology, 3*, 513-522.

Knobelspiesse, K.D., Cairns, B., Schmid, B., Román, M., & Schaaf, C.B. (2008). Surface BRDF estimation from an aircraft compared to MODIS and ground estimates at the Southern Great Plains site. *Journal of Geophysical Research-Atmospheres, 113*, D20, doi:10.1029/2008JD010062.

Kotchenova, S.Y., Vermote, E.F., Matarrese, R., & Klemm, F.J. (2006). Validation of a vector version of the 6S radiative transfer code for atmospheric correction of satellite data. Part I: Path Radiance. *Applied Optics, 45*, 6726-6774.

718   Lacaze, R., Chen, J.M., Roujean, J.-L., & Leblanc, S.G. (2002). Retrieval of vegetation
719 clumping index using hot spot signatures measured by POLDER instrument. *Remote Sensing of*
720 *Environment, 79*, 84-95.

721   Leroy, M., Deuzé, J.L., Bréon, F.M., Hautecoeur, O., Herman, M., Buriez, J.C., Tanré, D.,
722 Bouffié, S., Chazette, P., & Roujean, J.-L. (1997). Retrieval of atmospheric properties and sur-
723 face bidirectional reflectances over land from POLDER/ADEOS. *Journal of Geophysical Re-*
724 *search, 102*, 17023-17037.

725   Lewis, P. (1995). The utility of kernel-driven BRDF models in global BRDF and albedo stu-
726 dies. In, *Proceedings of the International Geoscience and Remote Sensing Symposium,*
727 *IGARSS'95* (pp. 1186-1188). Florence, Italy: IEEE International.

728   Li, X., Gao, F., Wang, J., & Strahler, A.H. (2001). A priori knowledge accumulation and its
729 application to linear BRDF model inversion. *Journal of Geophysical Research, 106*, 11925-
730 11935, doi:10.1029/2000JD900639.

731   Li, X.W., & Strahler, A.H. (1992). Geometric-optical bidirectional reflectance modeling of
732 the discrete crown vegetation canopy - Effect of crown shape and mutual shadowing. *IEEE*
733 *Transactions on Geoscience and Remote Sensing, 30*, 276-292.

734   Liang, S., Fang, H.L., Chen, M.Z., Shuey, C.J., Walthall, C., Daughtry, C., Morisette, J.,
735 Schaaf, C.B., & Strahler, A.H. (2002). Validating MODIS land surface reflectance and albedo
736 products: methods and preliminary results. *Remote Sensing of Environment, 83*, 149-162.

737   Liu, J., Schaaf, C.B., Strahler, A.H., Jiao, Z., Shuai, Y., Zhang, Q., Román, M., Augustine,
738 J.A., & Dutton, E.G. (2009). Validation of Moderate Resolution Imaging Spectroradiometer
739 (MODIS) albedo retrieval algorithm: Dependence of albedo on solar zenith angle. *Journal of*
740 *Geophysical Research-Atmospheres, 114*, D01106, doi:10.1029/2008JD009969.

741   Lucht, W., Schaaf, C.B., & Strahler, A.H. (2000). An algorithm for the retrieval of albedo
742 from space using semi-empirical BRDF models. *IEEE Transactions on Geoscience and Remote*
743 *Sensing, 38*, 977-998.

744   Lyapustin, A., Gatebe, C.K., Kahn, R., Brandt, R., Redemann, J., Russell, P., King, M.D.,
745 Pedersen, C.A., Gerland, S., Poudyal, R., Marshak, A., Wang, Y., Schaaf, C., Hall, D., & Kok-
746 hanovsky, A. (2009). Analysis of Snow BRF from ARCTAS Spring-2008 Campaign. *Atmos-*
747 *pheric Chemistry and Physics Discussions*, 21993-22040.

748   Moody, E.G., King, M.D., Schaaf, C.B., & Platnick, S. (2008). MODIS-derived spatially
749 complete surface albedo products: Spatial and temporal pixel distribution and zonal averages.
750 *Journal of Applied Meteorology and Climatology, 47*, 2879-2894.

32

751   Muller, J.-P., Preusker, R., Fischer, J., Zuhlke, M., Brockmann, C., & Regner, P. (2007).
752 ALBEDOMAP: MERIS land surface albedo retrieval using data fusion with MODIS BRDF and
753 its validation using contemporaneous EO and in situ data products,. In I. International (Ed.),
754 *Proceedings of the International Geoscience and Remote Sensing Symposium, IGARSS'07* (pp.
755 2404-2407). Barcelona, Spain.

756   NRSA (2003). IRS-P6 (AWIFS) Data User's Handbook. In G.o.I. Department of Space
757 (Ed.) (p. 142): National Remote Sensing Agency.

758   Pelgrum, H., Schmugge, T., Rango, A., Ritchie, J., & Kustas, W. (2000). Length scale anal-
759 ysis of surface albedo, temperature and NDVI in a desert grassland. *Water Resources Research,*
760 *36*, 1757-1765.

761   Pinty, B., Taberner, M., Haemmerle, V.R., Paradise, S.R., Vermote, E., Verstraete, M., Go-
762 bron, N., & Widlowski, J.-L. (2010). Global scale comparison of MISR and MODIS land surface
763 albedos. *Journal of Climate*, 10.1175/2010JCLI3709.1.

764   Pinty, B., Widlowski, J.-L., Gobron, N., Verstraete, M.M., & Diner, D.J. (2002). Uniqueness
765 of multiangular measurements -- Part I: An indicator of subpixel surface heterogeneity from
766 MISR. *IEEE Transactions on Geoscience and Remote Sensing, 40* 1560-1573.

767   Privette, J.L., Asner, G.P., Conel, J., Huemmrich, F.K., Olson, R., Rango, A., Rahman, A.F.,
768 Thome, K., & Walter-Shea, E.A. (2000). The EOS prototype validation exercise (PROVE) at
769 Jornada - Overview and lessons learned. *Remote Sensing of Environment, 74*, 1-12.

770   Privette, J.L., Eck, T.F., & Deering, D.W. (1997). Estimating spectral albedo and nadir ref-
771 lectance through inversion of simple BRDF models with AVHRR/MODIS-like data. *Journal of*
772 *Geophysical Research, 102*, 29529–29542.

773   Privette, J.L., Emery, W.J., & Schimel, D.S. (1996). Inversion of a vegetation reflectance
774 model with NOAA AVHRR data. *Remote Sensing of Environment, 58*, 187-200.

775   Privette, J.L., Tian, Y., Roberts, G., Scholes, R.J., Wang, Y., Caylor, K., & Mukelabai, M.
776 (2004). Structural characterization and relationships in Kalahari woodlands and savannas. *Global*
777 *Change Biology, 10*, 281-291.

778   Qin, W., & Gerstl, S.A.W. (2000). 3-D scene modeling of Jornada semi-desert vegetation
779 cover and its radiation regime. *Remote Sensing of Environment, 74*, 145-165.

780   Román, M.O., Schaaf, C.B., Lewis, P., Gao, F., Anderson, G.P., Privette, J.L., Strahler,
781 A.H., Woodcock, C.E., & Barnsley, M. (2010). Assessing the coupling between surface albedo
782 derived from MODIS and the fraction of diffuse skylight over spatially-characterized landscapes.
783 *Remote Sensing of Environment, 114*, 738-760, doi:10.1016/j.rse.2009.11.014.

784   Román, M.O., Schaaf, C.B., Yang, X., Woodcock, C.E., Strahler, A.H., Braswell, R.H., Cur-
785   tis, P.S., Davis, K.J., D., D., Gu, L., Goulden, M.L., Hollinger, D.Y., Kolb, T.E., Meyers, T.P.,
786   Munger, J.W., Privette, J.L., Richardson, A.D., Wilson, T.B., & Wofsy, S.C. (2009). The MOD-
787   IS (Collection V005) BRDF/albedo product: Assessment of spatial representativeness over fo-
788   rested landscapes. *Remote Sensing of Environment, 113*, 2476-2498, 10.1016/j.rse.2009.07.009.

789   Ross, J. (1981). *The Radiation Regime and Architecture of Plant Stands*. Norwell, Mass.:
790   The Hague: Dr. W. Junk Publishers.

791   Roujean, J., Leroy, M., & Deschanms, P. (1992). A bidirectional reflectance model of the
792   Earth's surface for the correction of remote sensing data. *Journal of Geophysical Research, 97*,
793   20,455-420,468.

794   Roy, D.P., Ju, J., Lewis, P., Schaaf, C.B., Gao, F., Hansen, M., & Lindquist, E. (2008). Mul-
795   ti-temporal MODIS–Landsat data fusion for relative radiometric normalization, gap filling, and
796   prediction of Landsat data *Remote Sensing of Environment, 112*, 3112-3130.

797   Russell, C.A., Irons, J.R., & Dabney, P.W. (1997a). Bidirectional reflectances of selected
798   BOREAS sites from multiangle airborne data. *Journal of Geophysical Research, 102(D24)*,
799   25,505-529,516.

800   Russell, C.A., Irons, J.R., & Dabney, P.W. (1997b). Bidirectional reflectances of selected
801   BOREAS sites from multiangle airborne data. *Journal of Geophysical Research, 102*, 29505-
802   29516.

803   Russell, P.B., Livingston, J.M., Hignett, P., Kinne, S., Wong, J., Chien, A., Bergstrom, R.,
804   Durkee, P., & Hobbs, P.V. (1999). Aerosol-induced radiative flux changes off the United States
805   mid-Atlantic coast: Comparison of values calculated from sunphotometer and in situ data with
806   those measured by airborne pyranometer. *Journal of Geophysical Research, 104*, 2289-2308.

807   Rutan, D., Rose, F.G., Román, M., Manalo-Smith, N., Schaaf, C., & Charlock, T. (2009).
808   Development and assessment of broadband surface albedo from CERES clouds and radia-tion
809   swath data product. *Journal of Geophysical Research, 114*, D08125,
810   doi:10.1029/2008JD010669.

811   Salomon, J.G., Schaaf, C.B., Strahler, A.H., Gao, F., & Jin, Y.F. (2006). Validation of the
812   MODIS bidirectional reflectance distribution function and albedo retrievals using combined ob-
813   servations from the Aqua and Terra platforms. *IEEE Transactions on Geoscience and Remote
814   Sensing, 44*, 1555-1565.

815   Sandmeier, S., Muller, C., Hosgood, B., & Andreoli, G. (1998). Physical mechanisms in
816   hyperspectral BRDF data of grass and watercress. *Remote Sensing of Environment, 66*, 222-233.

817   Schaaf, C.B., Gao, F., Strahler, A.H., Lucht, W., Li, X., Tsang, T., Strugnell, N.C., Zhang,
818 X., Jin, Y., Muller, J.-P., Lewis, P., Barnsley, M., Hobson, P., Disney, M., Roberts, G., Dunder-
819 dale, M., Doll, C., d'Entremont, R., Hu, B., Liang, S., Privette, J.L., & Roy, D.P. (2002). First
820 operational BRDF, albedo and nadir reflectance products from MODIS. *Remote Sensing of Envi-*
821 *ronment, 83*, 135-148.

822   Schaaf, C.B., Liu, J., Gao, F., & Strahler, A.H. (2011). MODIS albedo and reflectance ani-
823 sotropy products from Aqua and Terra. In B. Ramachandran, C. Justice & M. Abrams (Eds.),
824 *Land Remote Sensing and Global Environmental Change: NASA's Earth Observing System and*
825 *the Science of ASTER and MODIS* (p. 873): Springer-Cerlag.

826   Schaaf, C.B., Martonchik, J., Pinty, B., Govaerts, Y., Gao, F., Lattanzio, A., Liu, J., Strahler,
827 A.H., & Taberner, M. (2008). Retrieval of surface albedo from satellite sensors. In S. Liang
828 (Ed.), *Advances in Land Remote Sensing: System, Modeling, Inversion and Application* (pp. 219-
829 243): Springer.

830   Sellers, P.J., Hall, F.G., Asrar, G., Strebel, D.E., & Murphy, R.E. (1988). The first ISLSCP
831 field experiment (FIFE)
832   *Bulletin of the American Meteorological Society, 69*, 22-27.

833   Sellers, P.J., Hall, F.G., Asrar, G., Strebel, D.E., & Murphy, R.E. (1992). An overview of the
834 First International Satellite Land Surface Climatology Project (ISLSCP) Field Experiment
835 (FIFE). *Journal of Geophysical Research, 97*, 18,345-341,8371.

836   Strugnell, N., Lucht, W., & Schaaf, C.B. (2001). A global albedo data set derived from
837 AVHRR data for use in climate simulations. *Geophysical Research Letters, 28*, 191-194.

838   Susaki, J., Yasuoka, Y., Kajiwara, K., Honda, Y., & Hara, K. (2007). Validation of MODIS
839 albedo products of paddy fields in Japan. *IEEE Transactions on Geoscience and Remote Sens-*
840 *ing, 45*, 206-217.

841   Swap, R.J., Annegarn, H.J., & Otter, L. (2002). Southern African Regional Science Initiative
842 (SAFARI 2000): Summary of science plan. *South African Journal of Science, 98*, 119-124.

843   Taberner, M., Pinty, B., Govaerts, Y., Liang, S., Verstraete, M.M., Gobron, N., & Widlows-
844 ki, J.L. (2010). Comparison of MISR and MODIS land surface albedos: Methodology. *Journal of*
845 *Geophysical Research, 115*, doi:10.1029/2009JD012665.

846   Tucker, C.J. (1979). Red and photographic infrared linear combinations for monitoring ve-
847 getation. *Remote Sensing of Environment, 8*, 127-150.

848   Vermote, E.F., Tanré, D., Deuze, J.L., Herman, M., & Morcrette, J.-J. (1997). Second Simu-
849   lation of the Satellite Signal in the Solar Spectrum, 6S: an overview, Geoscience and Remote
850   Sensing. *IEEE Transactions on Geoscience and Remote Sensing, 35*, 675-686.

851   Walthall, C., Roujean, J.-L., & Morisette, J. (2000). Field and landscape BRDF optical wa-
852   velength measurements: Experience, techniques and the future. *Remote Sensing Reviews, 18*,
853   503-531.

854   Wanner, W., Li, X., & Strahler, A.H. (1995). On the Derivation of Kernels for Kernel-
855   Driven Models of Bidirectional Reflectance. *Journal of Geophysical Research-Atmospheres,
856   100*, 21077-21089.

857   Wanner, W., Strahler, A.H., Hu, B., Lewis, P., Muller, J., Li, X., Schaaf, C.B., & Barnsley,
858   M. (1997). Global retrieval of bidirectional reflectance and albedo over land from EOS MODIS
859   and MISR data: Theory and algorithm. *Journal of Geophysical Research, 102*, 17143-17161.

860   Waring, R.H., & Peterson, D.L. (1994). Oregon Transect Ecosystem Research (OTTER)
861   Project. *Ecological Applications, 4*, 210-211.

862   Widlowski, J.-L., Pinty, B., Gobron, N., Verstraete, M., & Davis, A.B. (2001). Characteriza-
863   tion of surface heterogeneity detected at the MISR/TERRA subpixel scale. *Geophysical Re-
864   search Letters, 28*, 4639-4642.

865   Zhang, Q. (2008). A Global Spatially and Temporarily Complete Reflectance Anisotropy
866   Database to Improve Surface Characterization for Albedo Modeling. In, *PhD Thesis, Department
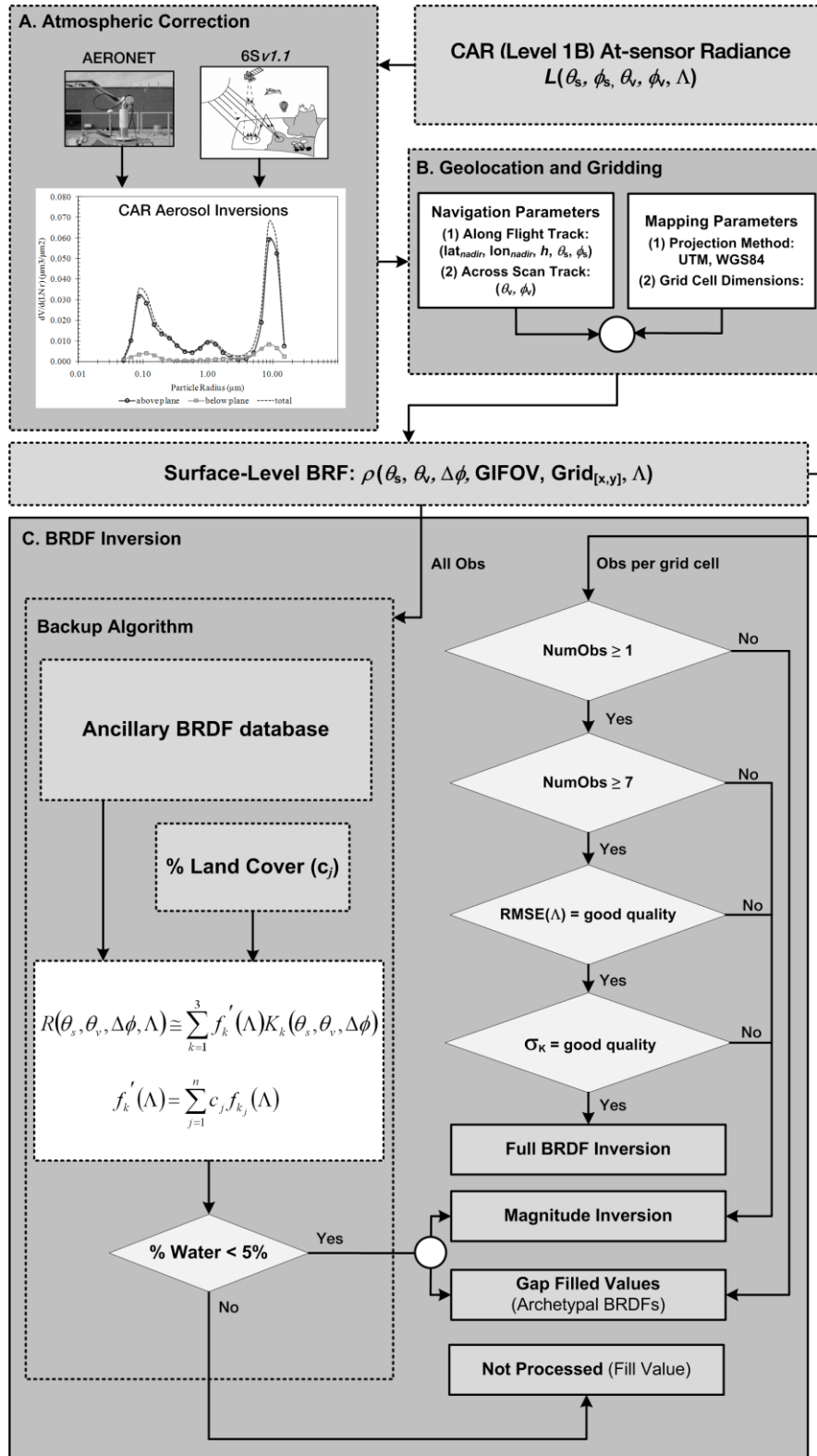867   of Geography and Environment* (p. 155). Boston, MA: Boston University.
868
869

Figures

2   Fig. 1. Processing and data flow diagram illustrating the production of spatially-distributed BRDF retrievals from
3   CAR. The algorithm has three main functional components: (a.) atmospheric correction, (b.) geolocation and grid-
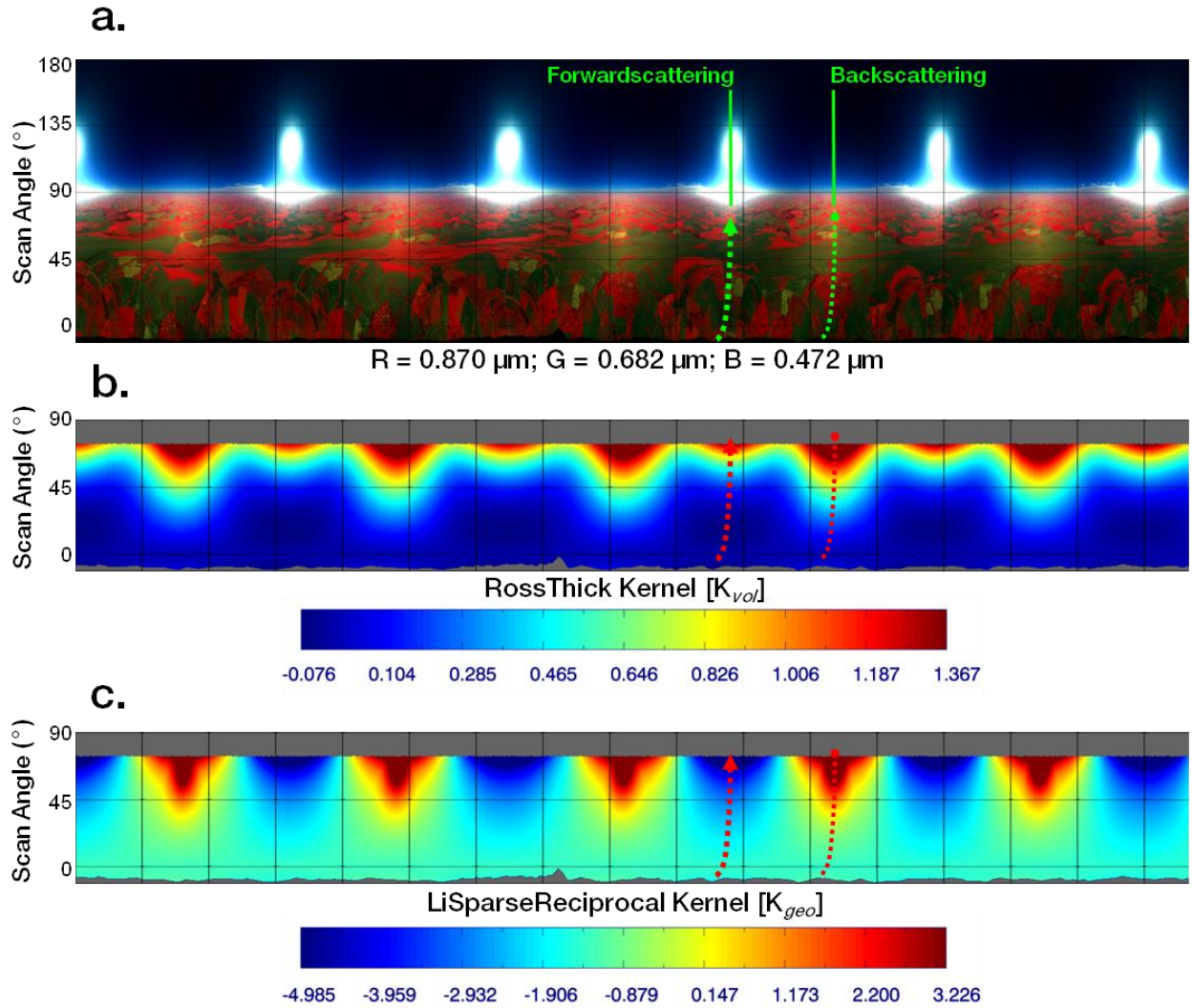4   ding, and (c.) BRDF inversion.
5

a.

Forwardscattering   Backscattering

R = 0.870 μm; G = 0.682 μm; B = 0.472 μm

b.

RossThick Kernel [K_{vol}]

-0.076 0.104 0.285 0.465 0.646 0.826 1.006 1.187 1.367

c.

LiSparseReciprocal Kernel [K_{geo}]

-4.985 -3.959 -2.932 -1.906 -0.879 0.147 1.173 2.200 3.226

Fig 2. Flight #1928 segment corresponding to a 12 minute period when the Cloud Absorption Radiometer (CAR) was flown at 2.0 km AGL. (a.) False-color surface BRF composite (atmospherically-corrected) for CAR scan angles ranging from zenith to nadir. The five solar disks in full view define the region of forwardscattering (i.e., sun oppo-site to the CAR instrument) where the presence of specular reflection and transmission of light through the edges of the canopies reaches a maximum. Note the bright areas along the surface located in the mid-regions between solar disks. This is the backscattering, or antisolar or hotspot, direction where all shadows are hidden. The dotted arrows correspond to a transect along the principal plane starting in the backscattering and ending in the forwardscattering direction. Corresponding transects for the RossThick (K_{vol}) and the LiSparseReciprocal (K_{geo}) kernels (b. and c., re-spectively) are also shown.
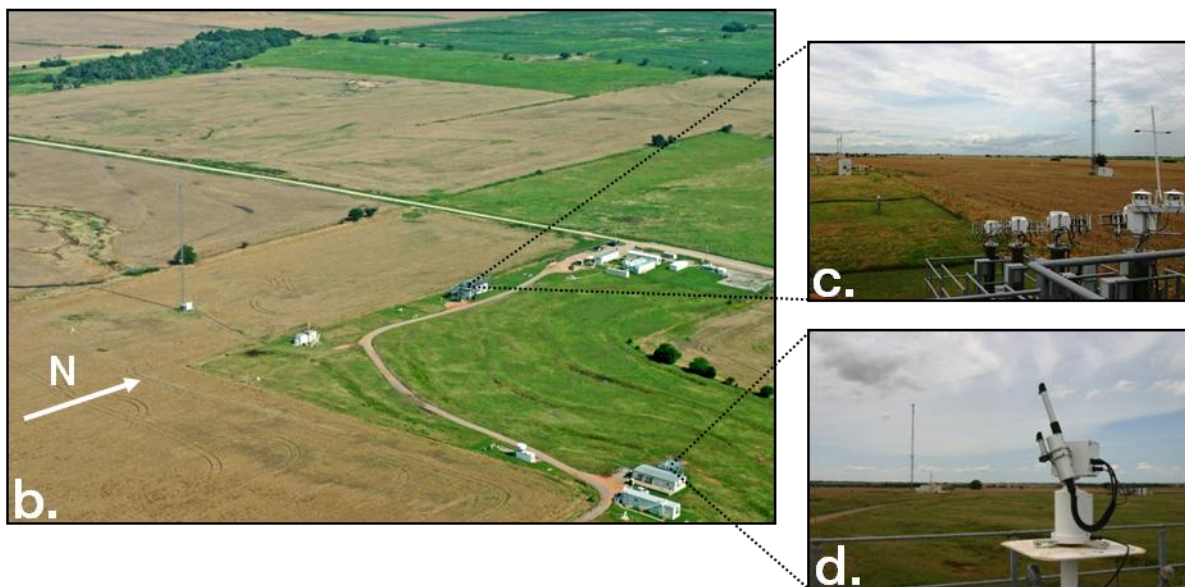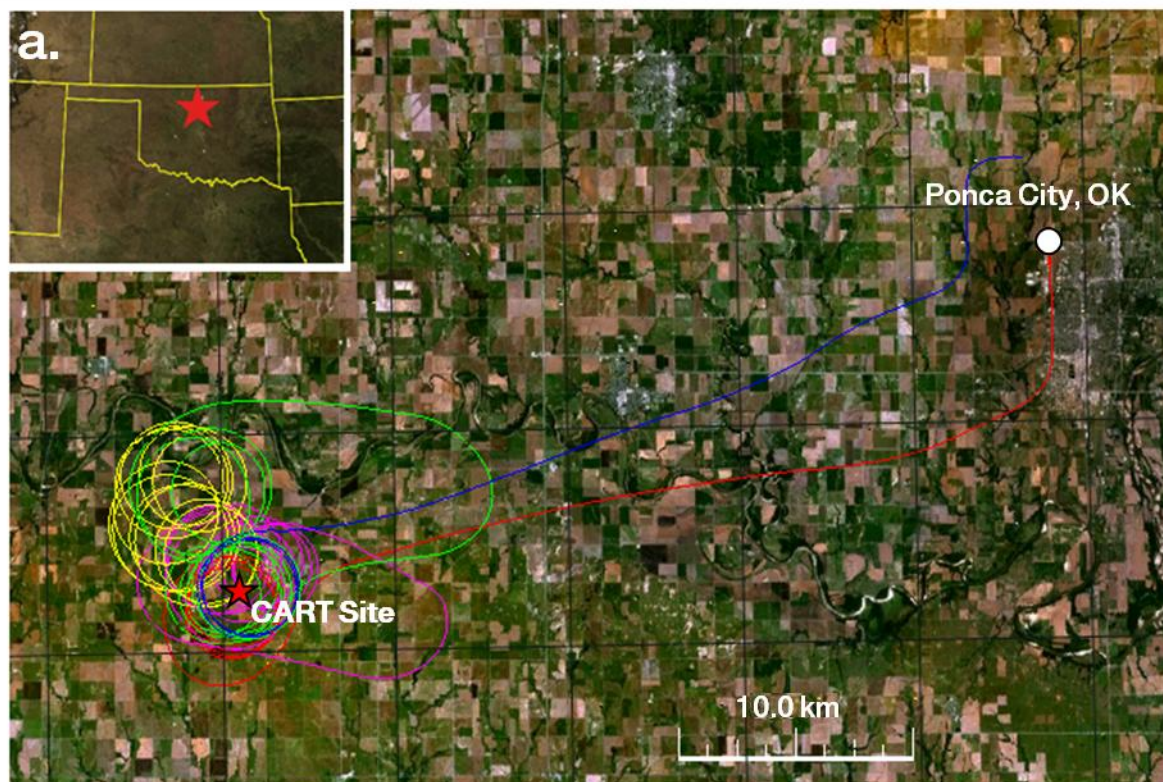
2

Fig. 3 (a.) Flight #1928 flight track over the U.S. Southern Great Plains Cloud and Radiation Testbed (CART) Site (24 June 2007). The multi-colored track shows the time sequence, with red representing the first 30 minutes of the flight, and then a series of 14-minute time steps starting with magenta, yellow, green, and blue. (b.) Bird's eye view of the CART site taken during Flight #1922 (19 June 2007). (c.) Facing southwest atop the Radiometric Calibration Facility, overlooking the upward-facing pyranometers and the 60 meter radiation tower (20 June 2007). (d.) Facing west atop the Guest Instrument Facility, overlooking the AERONET sun photometer (20 June 2007).
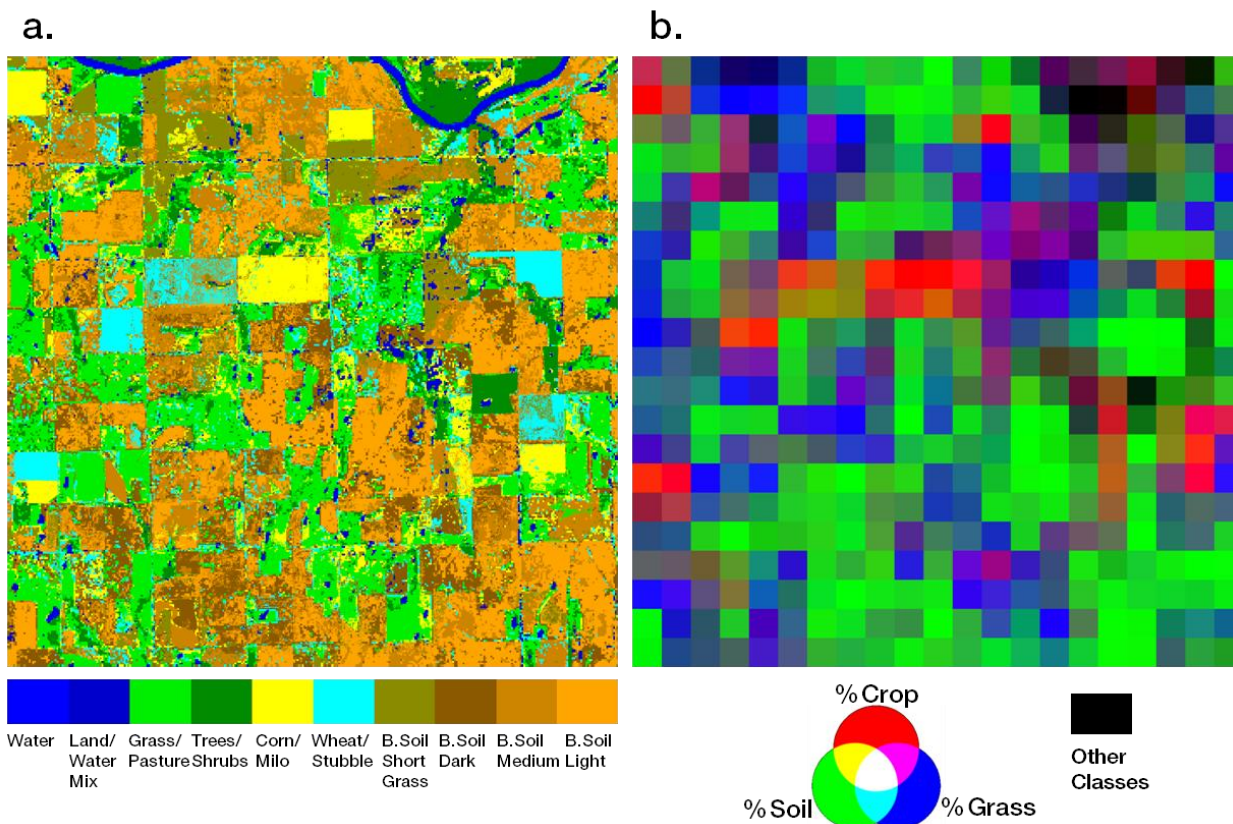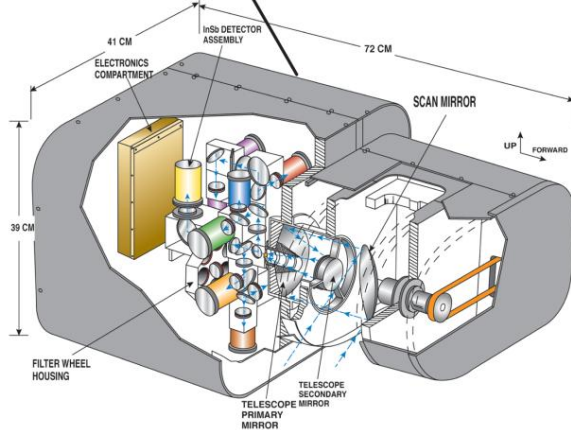
3

a.

b.

Water | Land/Water Mix | Grass/Pasture | Trees/Shrubs | Corn/Milo | Wheat/Stubble | B.Soil Short Grass | B.Soil Dark | B.Soil Medium | B.Soil Light

% Crop
% Soil
% Grass
Other Classes

Fig 4. (a.) Land cover types in a 10 km^2 area surrounding the U.S. Southern Great Plains Cloud and Radiation Testbed (CART) during late June, 2007. The effective spatial resolution of this land cover map is 2.4 m. The overall classification accuracy is ~92% relative to ground-based surveys. The most dominant land cover type (at 55%) is bare soil in various conditions (dark, light, and partially vegetated), followed by pasture/grassland (18%) and corn/milo fields (9%). (b.) Fractional cover estimates (%) of crop (including corn/milo and wheat/stubble classes), pasture, and bare soils, using a 500 m grid cell size.
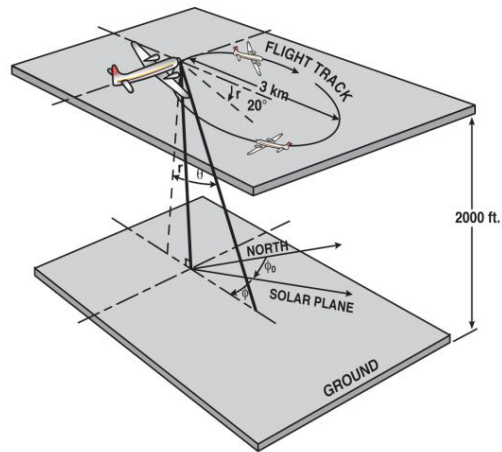
a. Jetstream-31 Aircraft

c. BRDF Flight Track

FLIGHT TRACK
3 km
20°
2000 ft.
NORTH
φ_0
SOLAR PLANE
GROUND

b. CAR Schematic

41 CM
InSb DETECTOR ASSEMBLY
72 CM
ELECTRONICS COMPARTMENT
SCAN MIRROR
UP FORWARD
39 CM
FILTER WHEEL HOUSING
TELESCOPE SECONDARY
TELESCOPE MIRROR
PRIMARY MIRROR

d. Cloud Absorption Radiometer (CAR) Parameters

Angular scan range	190°
Instantaneous field of view	17.5 mrad (1°)
Pixels per scan line	382
Scan rate	1.67 scan lines per second (100 rpm)
Spectral channels (μm; bandwidth (FWHM))	14 [a] (8 continuously sampled and last six in filter wheel): 0.340(0.009), 0.381(0.006), 0.472(0.021), 0.682(0.022), 0.870(0.022), 1.036(0.022), 1.219(0.022), 1.273(0.023), 1.556(0.032), 1.656(0.045), 1.737(0.040), 2.103(0.044), 2.205(0.042), 2.302(0.043)

Fig. 5. (a.) The N22746 aircraft registered to Sky Research Inc. (USA), also known as Jetstream-31 (J-31) in Ponca City Airport, Oklahoma, USA during the 2007 Cloud and Land Surface Interaction Campaign (CLASIC). (b.) Schematic of NASA's Cloud Absorption Radiometer (CAR), which is mounted in the nose cone of the J-31. The CAR measured the spectral and angular distribution of scattered light by clouds and aerosols, and obtained good imagery of clouds and Earth surface features over many areas in the U.S. Southern Great Plains Cloud and Radiation Testbed (CART) Site. (c.) Illustration of a clockwise circular flight track that was used for measuring surface-level bidirectional reflectances. (d.) The CAR has 14 narrow spectral bands between 0.34 and 2.30 µm, and flew 11 missions during CLASIC (Gatebe et al., 2003; King et al., 1986).

.

Table 1. RTLSR BRDF model parameters, $f_{iso}(\Lambda)$, $f_{vol}(\Lambda)$, $f_{geo}(\Lambda)$, and best-fit RMSE results derived for four discreet wavelengths, from 0.472 μm to 1.219 μm, for each of the representative land covers classes identified across the CART site during the CLASIC experiment.

| Surface Type	RTLSR BRDF(0.472 μm)				RTLSR BRDF(0.682 μm)			
	fiso(Λ)	*fvol*(Λ)	*fgeo*(Λ)	RMSE(Λ)	*fiso*(Λ)	*fvol*(Λ)	*fgeo*(Λ)	RMSE(Λ)
Grass/Pasture	0.0303	0.0553	0.0022	0.0108	0.0579	0.0941	0.0058	0.0213
Trees/Shrubs	0.0308	0.0433	0.0030	0.0112	0.0610	0.0649	0.0065	0.0224
Corn/Milo	0.0335	0.0692	0.0005	0.0138	0.0666	0.1074	0.0026	0.0265
Wheat/Stubble	0.0437	0.0419	0.0043	0.0105	0.0916	0.0672	0.0093	0.0240
Bare Soil/Short Grass	0.0500	0.0490	0.0019	0.0124	0.1021	0.0723	0.0031	0.0260
Bare Soil Dark	0.0390	0.0470	0.0014	0.0100	0.0922	0.0839	0.0045	0.0234
Bare Soil Medium	0.0458	0.0544	0.0032	0.0089	0.1050	0.1046	0.0093	0.0191
Bare Soil Light	0.0497	0.0596	0.0027	0.0083	0.1282	0.1253	0.0150	0.0222
Surface Type	RTLSR BRDF(0.870 μm)				RTLSR BRDF(1.219 μm)			
	fiso(Λ)	*fvol*(Λ)	*fgeo*(Λ)	RMSE(Λ)	*fiso*(Λ)	*fvol*(Λ)	*fgeo*(Λ)	RMSE(Λ)
Grass/Pasture	0.3777	0.1108	0.0023	0.0442	0.3357	0.2483	0.0181	0.0378
Trees/Shrubs	0.3444	0.1497	0.0082	0.0479	0.3300	0.2667	0.0268	0.0473
Corn/Milo	0.3712	0.1315	0.0051	0.0535	0.3306	0.2754	0.0136	0.0431
Wheat/Stubble	0.3291	0.2026	0.0154	0.0648	0.3430	0.2559	0.0340	0.0425
Bare Soil/Short Grass	0.3299	0.0890	0.0207	0.0486	0.3663	0.1787	0.0424	0.0419
Bare Soil Dark	0.3201	0.1860	0.0117	0.0504	0.3194	0.2437	0.0157	0.0399
Bare Soil Medium	0.2911	0.1889	0.0184	0.0394	0.3284	0.2285	0.0346	0.0320
Bare Soil Light	0.2972	0.1612	0.0237	0.0387	0.3435	0.2217	0.0369	0.0342
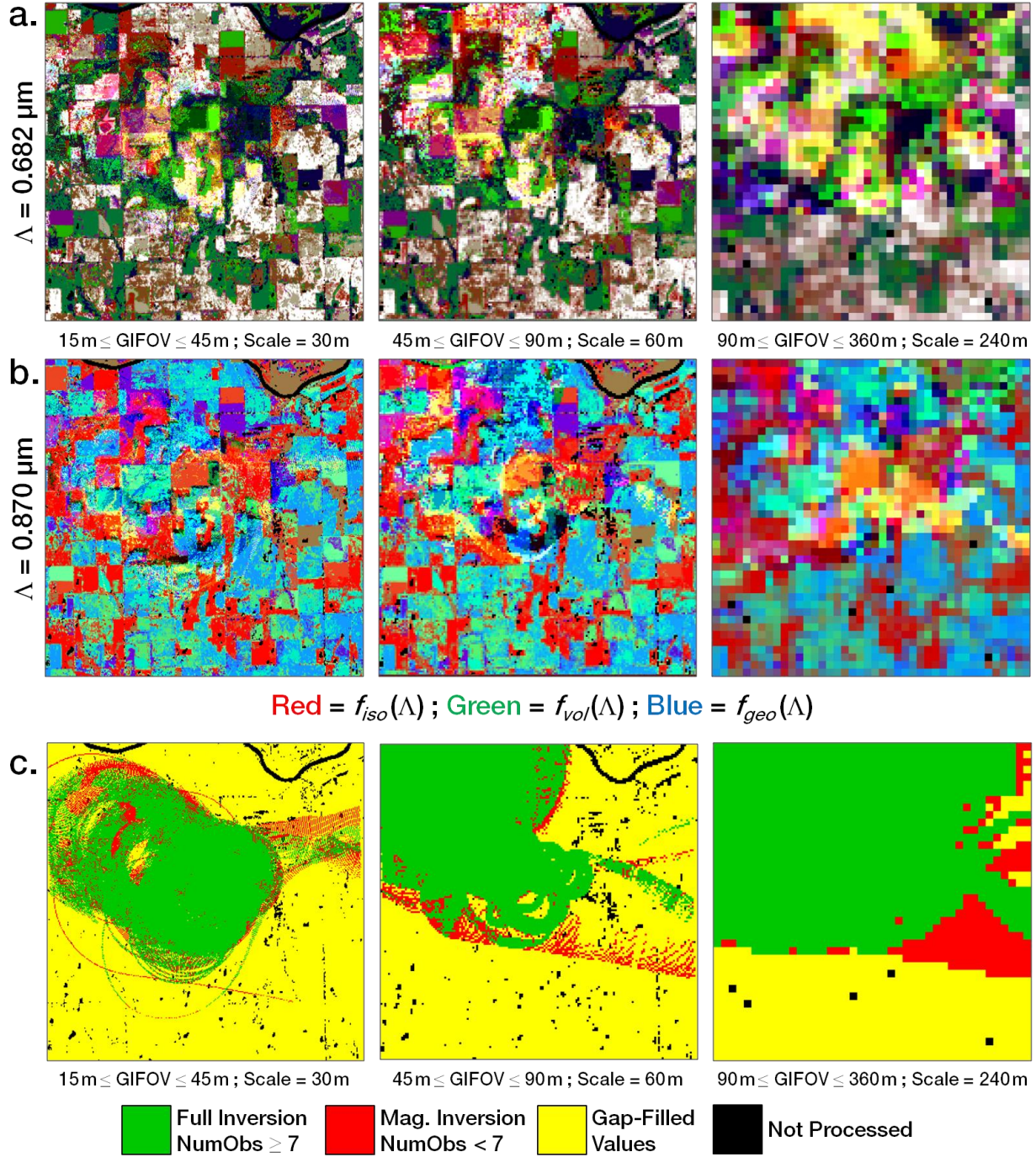
Fig. 6. Cloud Absorption Radiometer (CAR) RTLSR model parameters describing the BRDF at (a.) Λ = 0.682 μm and (b.) Λ = 0.870 μm for a 10 km^2 area surrounding the U.S. Southern Great Plains Cloud and Radiation Testbed (CART) site during late June, 2007. Each product is defined by a distinct cell size (or scale) (i.e., 30 m, 60 m, and 240 m) and GIFOV range (i.e., 15 m ≤ GIFOV ≤ 45 m, 45 m ≤ GIFOV ≤ 90 m, and 90 m ≤ GIFOV ≤ 360 m). (c.) Per-pixel band-specific BRDF model inversion quality equivalent to the MODIS BRDF/Albedo quality Level 3 product (MCD43A2).
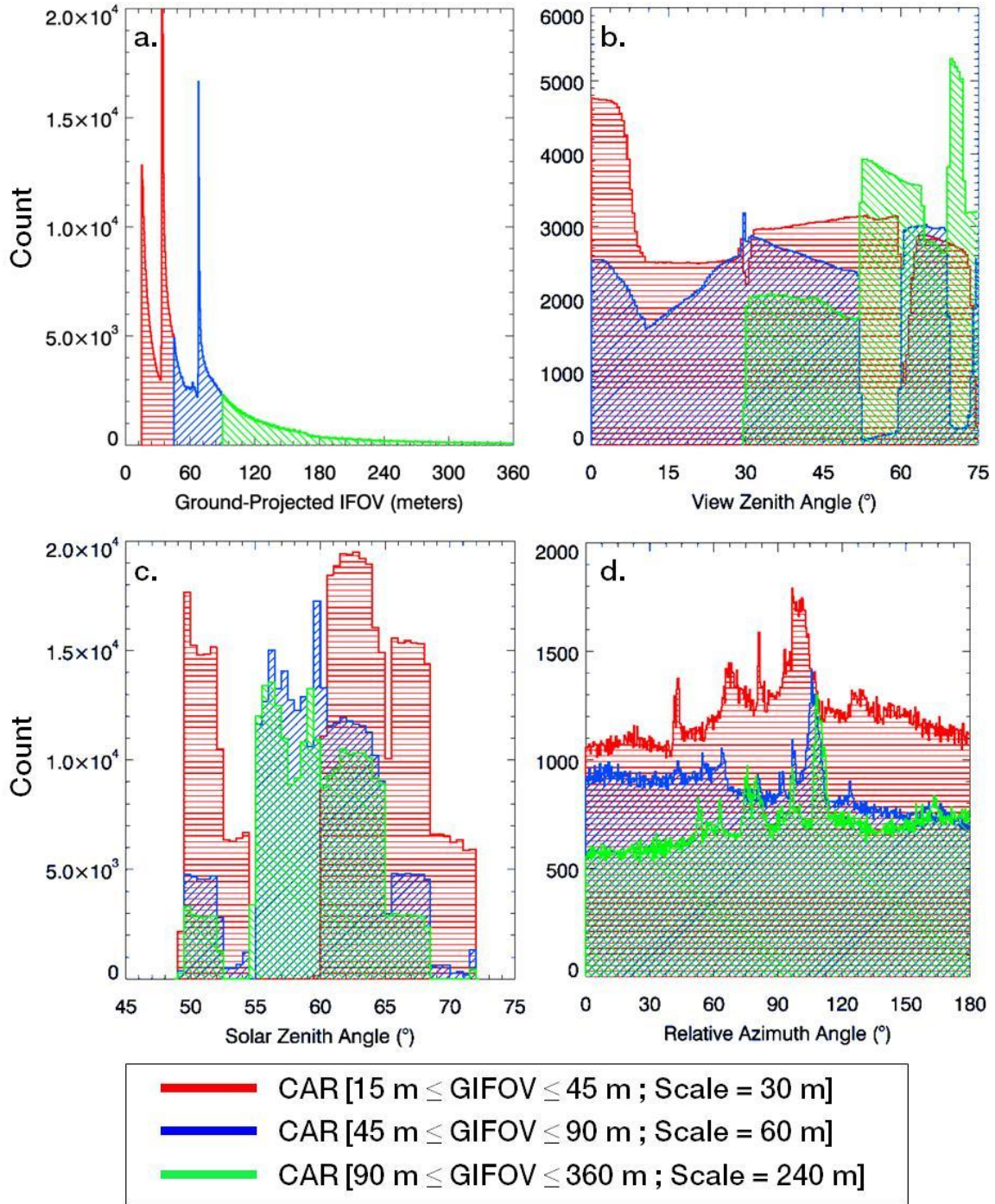
Fig. 7. Distribution of Flight #1928 measurements for three different grids sizes equal to 30 m^2 (in red), 60 m^2 (in blue), and 240 m^2 (in green). (a.) Each grid consists of BRF data from Flight #1928 selected from a distinctive range of GIFOVs. Measurements are also shown as a function of: (b.) view zenith angle; (c.) solar zenith angle; and (d.) relative azimuth angle.
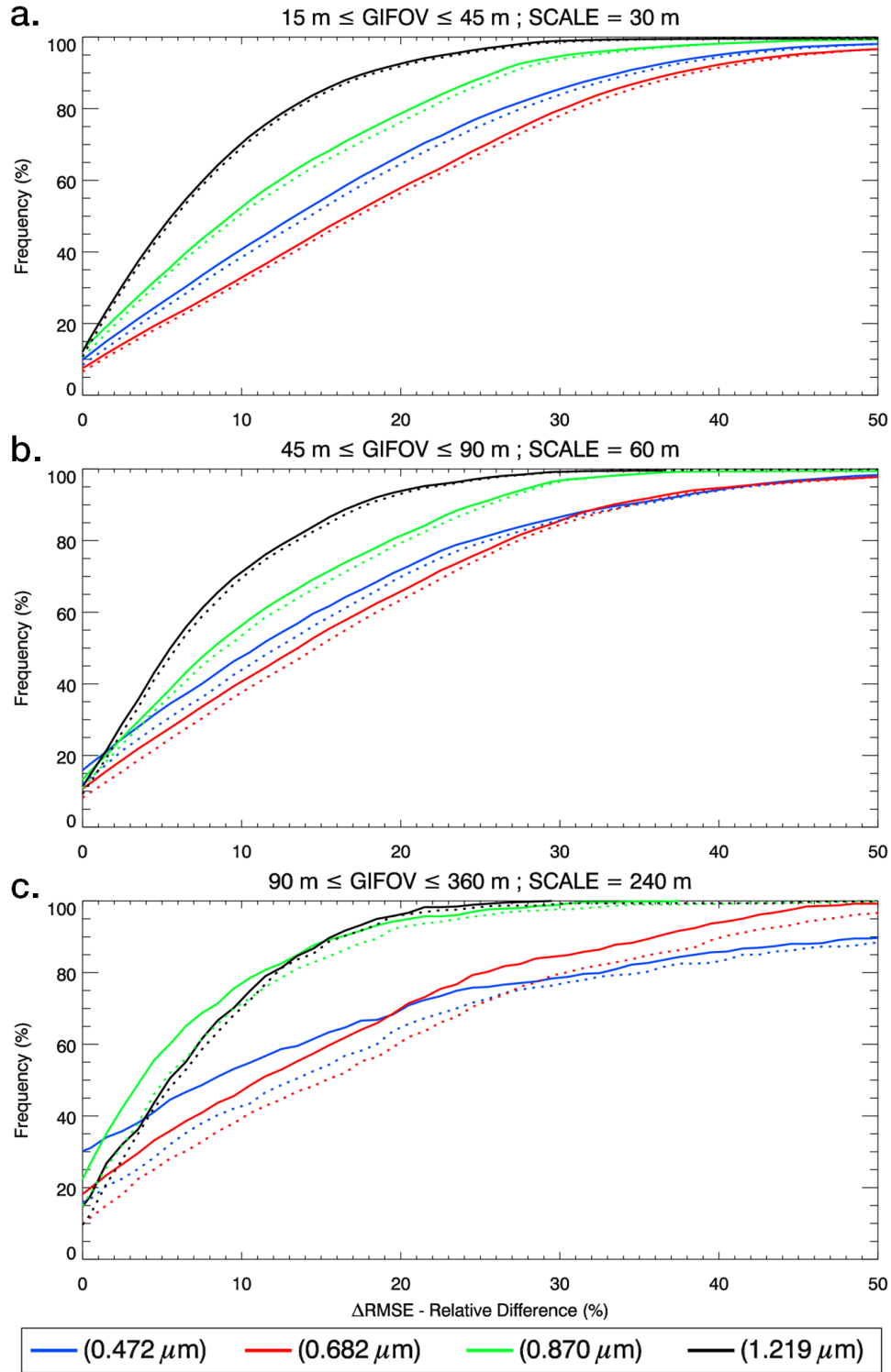
Fig, 8. Cumulative distribution of relative RMSE differences(%) in CAR-derived RossThick-LiSparseReciprocal BRDF model inversions for three grid cell sizes equal to 30 m (a.), 60 m (b.), and 240 m (c.); and for four discreet wavelengths from 0.472 μm to 1.219 μm. Each plot illustrates the robustness of Flight #1928 BRDF retrievals employing a priori archetypal BRDF shapes to describe the surface anisotropy as either: (1) a linear-mixture of different ecosystem types (solid lines); or (2) a single (or dominant) ecosystem type (dotted lines).

9

115   Table 2. Cumulative distribution of relative RMSE differences (%) in CAR-derived RossThick-LiSparseReciprocal
116   BRDF model inversions (as illustrated in Fig. 8) for three grid cell sizes equal to (a.) 30 m, (b.) 60 m, and (c.) 240
117   m, using four discreet wavelengths from 0.472 μm to 1.219 μm, and five frequency limits for ΔRMSE values ≤ 10%
118   to ≤ 50%. Numbers before and after each slash are for a priori archetypal BRDF retrievals employing the "linear-
119   mixture" and "dominant" assumptions, respectively.

A. CAR BRDF [15 m ≤ GIFOV ≤ 45 m ; Scale = 30 m] – % Frequency				
Wavelength	ΔRMSE ≤ 10%	ΔRMSE ≤ 20%	ΔRMSE ≤ 30%	ΔRMSE ≤ 40%	ΔRMSE ≤ 50%
Λ = 0.472μm	42.17% / 39.82%	68.13% / 65.68%	86.19% / 84.67%	95.33% / 94.66%	98.12% / 98.13%
Λ = 0.682μm	34.17% / 32.85%	59.05% / 57.60%	80.53% / 79.00%	92.70% / 91.84%	96.72% / 96.77%
Λ = 0.870μm	54.26% / 52.40%	79.72% / 77.43%	95.04% / 94.19%	98.27% / 98.22%	99.38% / 99.60%
Λ = 1.219μm	72.27% / 71.09%	93.11% / 92.46%	99.00% / 98.73%	99.53% / 99.64%	99.56% / 99.85%

B. CAR BRDF [45 m ≤ GIFOV ≤ 90 m ; Scale = 60 m] – % Frequency				
Wavelength	ΔRMSE ≤ 10%	ΔRMSE ≤ 20%	ΔRMSE ≤ 30%	ΔRMSE ≤ 40%	ΔRMSE ≤ 50%
Λ = 0.472μm	48.77% / 45.25%	72.89% / 71.00%	87.13% / 86.14%	94.62% / 94.30%	98.40% / 98.45%
Λ = 0.682μm	41.93% / 38.94%	66.90% / 64.53%	84.88% / 80.13%	94.29% / 90.31%	97.89% / 97.78%
Λ = 0.870μm	58.00% / 55.24%	82.27% / 80.36%	97.10% / 96.88%	99.36% / 99.52%	99.47% / 99.81%
Λ = 1.219μm	72.83% / 71.35%	94.33% / 93.69%	99.26% / 99.22%	99.53% / 99.79%	99.53% / 99.84%

C. CAR BRDF [90 m ≤ GIFOV ≤ 360 m ; Scale = 240 m] – % Frequency				
Wavelength	ΔRMSE ≤ 10%	ΔRMSE ≤ 20%	ΔRMSE ≤ 30%	ΔRMSE ≤ 40%	ΔRMSE ≤ 50%
Λ = 0.472μm	54.82% / 43.41%	70.88% / 65.68%	78.80% / 77.27%	85.87% / 83.64%	89.94% / 88.64%
Λ = 0.682μm	48.46% / 40.71%	71.45% / 62.04%	86.37% / 85.14%	94.86% / 94.72%	99.23% / 96.93%
Λ = 0.870μm	78.42% / 72.79%	94.96% / 93.03%	99.28% / 97.62%	100.00% / 99.15%	100.00% / 99.83%
Λ = 1.219μm	74.80% / 72.17%	96.71% / 96.28%	100.00% / 99.35%	100.00% / 99.35%	100.00% / 99.87%

120
121
122

CAR BRF [15 m ≤ GIFOV ≤ 45 m ; Scale = 30 m]

CAR BRF [45 m ≤ GIFOV ≤ 90 m ; Scale = 60 m]

CAR BRF [90 m ≤ GIFOV ≤ 360 m ; Scale = 240 m]

MCD43A1 BRF [250 m ≤ GIFOV ≤ 1000 m ; Scale = 500 m]

$\theta_v = -60.0°$ $\theta_v = -30.0°$ $\theta_v = 0.0°$ $\theta_v = 30.0°$ $\theta_v = 60.0°$

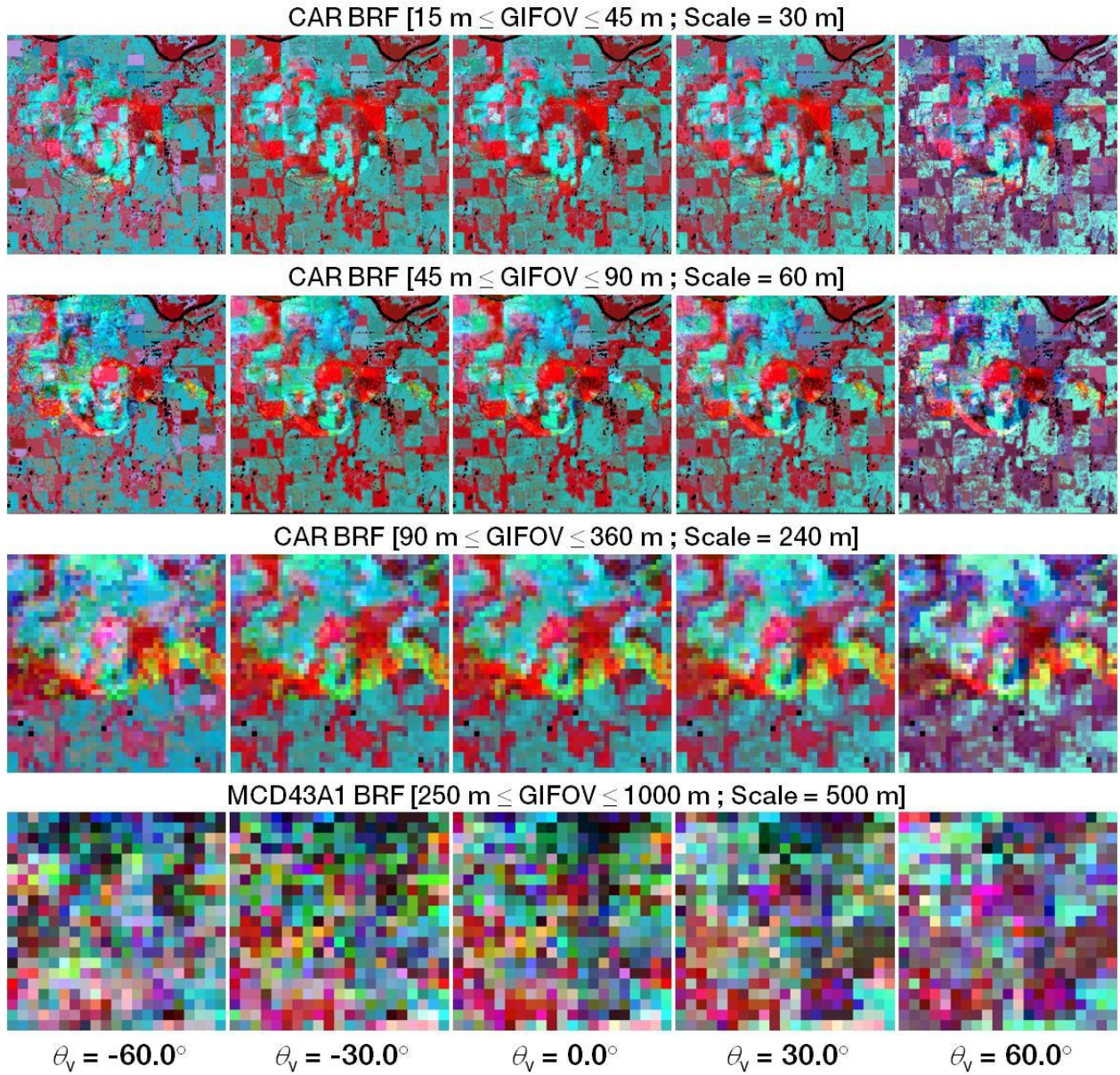Red = BRF(0.870 μm) ; Green = BRF(0.682 μm) ; Blue = BRF(0.472 μm)

123
124
125 Fig. 9. Principal plane surface BRF fields derived from CAR Flight #1928 and MODIS Collection 5 (MDC43A1)
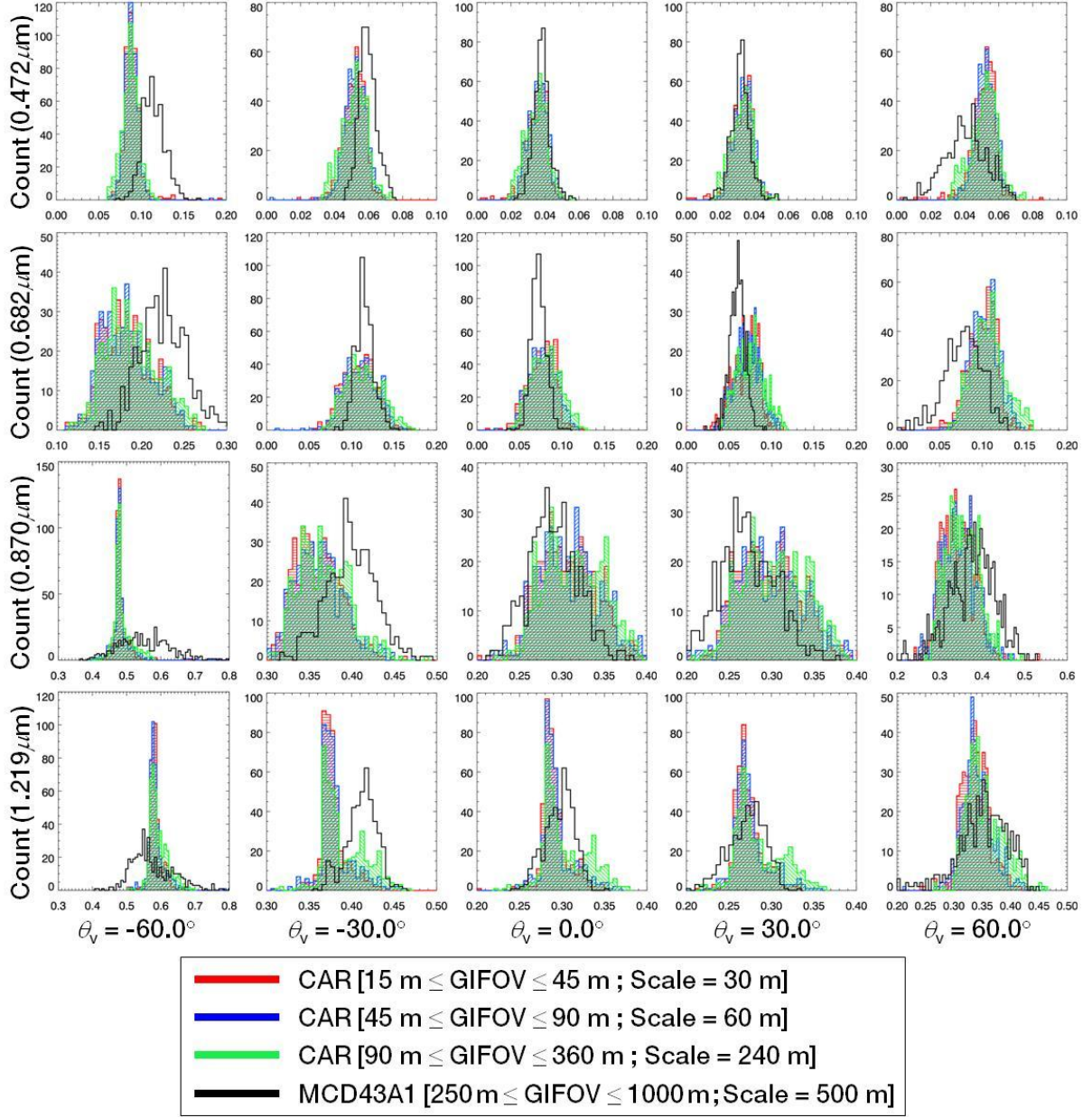126 BRDF model parameters over the CART site.
127
128
129

11

Fig. 10. Distribution of spatially distributed BRF retrievals from CAR and MCD43A1 BRDF model inversions for four discreet wavelengths from 0.472 μm (top) to 1.219 μm (bottom).

144   Table 3. Accuracy[a], precision[b], and uncertainty[c] (APU) values resulting from comparisons between CAR-derived
145   surface BRFs and MCD43A1 for each of the spatially-distributed BRDF fields examined in Fig. 10.

Band	VZA	CAR [15 m ≤ GIFOV ≤ 45 m; Scale = 30 m] vs. MCD43A1			CAR [45 m ≤ GIFOV ≤ 90 m; Scale = 60 m] vs. MCD43A1			CAR [90 m ≤ GIFOV ≤ 360 m; Scale = 240 m] vs. MCD43A1		
		Accuracy	Precision	Uncertainty	Accuracy	Precision	Uncertainty	Accuracy	Precision	Uncertainty
0.472μm	-60˚	-32.70%	20.99%	0.0313	-30.20%	20.49%	0.0380	**-29.63%**	**19.83%**	**0.0311**
0.472μm	-30˚	-17.71%	20.55%	0.1150	-17.47%	21.76%	0.0120	**-16.74%**	**19.85%**	**0.1120**
0.472μm	0˚	-11.18%	39.02%	0.0097	**-5.96%**	36.40%	0.0172	-13.38%	**26.18%**	**0.0082**
0.472μm	30˚	-7.95%	28.49%	0.0107	4.41%	28.19%	0.0217	**-2.06%**	**28.02%**	**0.0081**
0.472μm	60˚	**17.68%**	28.11%	0.0194	22.91%	29.80%	0.0314	18.92%	**27.94%**	**0.0178**
0.682μm	-60˚	-25.40%	24.93%	0.0580	-24.68%	24.92%	0.0591	**-22.12%**	**23.25%**	**0.0526**
0.682μm	-30˚	-9.14%	22.58%	0.0223	-9.48%	22.40%	0.0224	**-3.91%**	**20.57%**	**0.0219**
0.682μm	0˚	**1.18%**	34.31%	**0.0184**	3.96%	30.78%	0.0231	6.33%	**23.29%**	0.0205
0.682μm	30˚	16.66%	25.52%	**0.0209**	15.86%	27.63%	0.0280	16.13%	**23.47%**	0.0241
0.682μm	60˚	**17.94%**	47.66%	**0.0372**	26.97%	42.11%	0.0450	25.47%	**26.51%**	0.0426
0.870μm	-60˚	-33.51%	**12.10%**	0.1717	-33.62%	12.13%	0.1697	**-32.68%**	13.02%	**0.1673**
0.870μm	-30˚	-11.50%	**11.61%**	0.0567	-11.75%	12.86%	0.0582	**-9.46%**	12.30%	**0.0541**
0.870μm	0˚	4.26%	**14.34%**	**0.0477**	**2.92%**	24.84%	0.0536	6.60%	14.55%	0.0530
0.870μm	30˚	**6.90%**	16.80%	**0.0554**	11.40%	14.48%	0.0626	9.65%	**16.11%**	0.0611
0.870μm	60˚	11.63%	21.79%	0.0748	11.51%	21.47%	0.0831	**7.72%**	**19.52%**	**0.0705**
1.219μm	-60˚	-17.70%	8.58%	0.1141	-17.36%	8.96%	0.1133	**-16.31%**	**8.86%**	**0.1080**
1.219μm	-30˚	-9.12%	**6.76%**	0.0423	-8.90%	8.19%	0.0434	**-6.13%**	8.86%	**0.0403**
1.219μm	0˚	-2.51%	**8.35%**	**0.0252**	-4.76%	43.59%	0.0346	**1.28%**	11.16%	0.0352
1.219μm	30˚	4.08%	13.09%	0.0415	7.78%	15.52%	0.0412	**0.13%**	**10.66%**	**0.0289**
1.219μm	60˚	4.68%	**16.31%**	**0.0605**	0.53%	17.07%	0.0655	**0.25%**	17.03%	**0.0551**

146
147   [a] Accuracy = arithmetic mean(CAR – MODIS) × arithmetic mean(CAR)$^{-1}$ × 100 %
148   [b] Precision = standard deviation(CAR – MODIS) × arithmetic mean(CAR)$^{-1}$ × 100 %
149   [c] Uncertainty: Absolute RMSE = $\sqrt{\text{arithmetic mean(CAR - MODIS)}^2}$
150
151